HOST-GALAXY PROPERTIES OF 32 LOW-REDSHIFT SUPERLUMINOUS SUPERNOVAE FROM THE PALOMAR TRANSIENT FACTORY

D. A. PERLEY[1,2], R. M. QUIMBY[3,4], L. YAN[5], P. M. VREESWIJK[6], A. DE CIA[6,7], R. LUNNAN[2], A. GAL-YAM[6], O. YARON[6], A. V. FILIPPENKO[8], M. L. GRAHAM[8], R. LAHER[9], AND P. E. NUGENT[8,10]

[1] Dark Cosmology Centre, Niels Bohr Institute, University of Copenhagen, Juliane Maries Vej 30, DK-2100 København Ø, Denmark; dperley@dark-cosmology.dk
[2] Department of Astronomy, California Institute of Technology, MC 249-17, 1200 East California Blvd., Pasadena, CA 91125, USA
[3] Department of Astronomy, San Diego State University, San Diego, CA 92182, USA
[4] Kavli IPMU (WPI), UTIAS, The University of Tokyo, Kashiwa, Chiba 277-8583, Japan
[5] Infrared Processing and Analysis Center, California Institute of Technology, Pasadena, CA 91125, USA
[6] Department of Particle Physics and Astrophysics, Faculty of Physics, The Weizmann Institute of Science, Rehovot 76100, Israel
[7] European Southern Observatory, Karl-Schwarzschild-Strasse 2, D-85748 Garching bei München, Germany
[8] Department of Astronomy, University of California, Berkeley, CA 94720-3411, USA
[9] Spitzer Science Center, California Institute of Technology, MC 314-6, Pasadena, CA 91125, USA
[10] Lawrence Berkeley National Laboratory, 1 Cyclotron Rd., Berkeley, CA 94720, USA

ABSTRACT

We present ultraviolet through near-infrared photometry and spectroscopy of the host galaxies of all superluminous supernovae (SLSNe) discovered by the Palomar Transient Factory prior to 2013 and derive measurements of their luminosities, star formation rates, stellar masses, and gas-phase metallicities. We find that Type I (hydrogen-poor) SLSNe (SLSNe I) are found almost exclusively in low-mass ($M_* < 2 \times 10^9\,M_\odot$) and metal-poor ($12 + \log_{10}[O/H] < 8.4$) galaxies. We compare the mass and metallicity distributions of our sample to nearby galaxy catalogs in detail and conclude that the rate of SLSNe I as a fraction of all SNe is heavily suppressed in galaxies with metallicities $\gtrsim 0.5\,Z_\odot$. Extremely low metallicities are not required and indeed provide no further increase in the relative SLSN rate. Several SLSN I hosts are undergoing vigorous starbursts, but this may simply be a side effect of metallicity dependence: dwarf galaxies tend to have bursty star formation histories. Type II (hydrogen-rich) SLSNe (SLSNe II) are found over the entire range of galaxy masses and metallicities, and their integrated properties do not suggest a strong preference for (or against) low-mass/low-metallicity galaxies. Two hosts exhibit unusual properties: PTF 10uhf is an SLSN I in a massive, luminous infrared galaxy at redshift $z = 0.29$, while PTF 10tpz is an SLSN II located in the nucleus of an early-type host at $z = 0.04$.

Key words: galaxies: abundances – galaxies: dwarf – galaxies: photometry – supernovae: general

Supporting material: machine-readable tables

1. INTRODUCTION

The recently discovered observational class of "superluminous" supernovae (SLSNe) has complicated what was once a fairly straightforward view of the fates of massive stars in the local universe, in which all stars above $8\,M_\odot$ were thought to explode via a common mechanism of iron core collapse (see, e.g., Filippenko 1997, for a review). SLSNe have characteristic peak visual absolute magnitudes between -21 and -22.5 ($\sim 10^{10}\,L_\odot$; Gal-Yam 2012; Nicholl et al. 2015), making them much more luminous than typical core-collapse supernovae (CCSNe), which peak between -15 and -18 mag ($\sim 10^8$–$10^9\,L_\odot$; Richardson et al. 2002; Li et al. 2011.) Most SLSNe also evolve much more slowly and have higher peak temperatures than ordinary CCSNe, and the time-integrated bolometric radiative output of an SLSN may reach $\gtrsim 10^{51}$ erg, exceeding a typical CCSN by 2–3 orders of magnitude. This points to a much larger progenitor mass and may require a fundamentally different explosion mechanism.

The spectroscopic properties of SLSNe are diverse: they include events showing strong hydrogen emission throughout their observed evolution, events that show no hydrogen lines at any epoch, and intermediate cases of weak and/or transient hydrogen emission. Mirroring the classification scheme for ordinary SNe, SLSNe are classified as Type I (no hydrogen observed) or Type II (hydrogen observed); see Gal-Yam (2012) for a review of SLSN classes and properties.

Events showing narrow or intermediate-width hydrogen lines in their spectra (all of which are Type II by definition, and which represent the majority of events in this class) are simplest to accommodate physically, since the existence of these lines is direct evidence of interaction between SN ejecta and a dense surrounding medium (e.g., Moriya et al. 2013). This process permits the bulk kinetic energy of the outflow to be tapped and converted to electromagnetic radiation, helping to explain the large radiative output of these events and easing the fundamental energy requirements. Indeed, "ordinary" Type IIn SNe (SNe IIn) are the most luminous class of CCSNe and are thought to occur when SN ejecta collide with shells of material from previous eruptions (e.g., Schlegel 1990; Filippenko 1997; Kiewe et al. 2012). The underlying mechanism in SLSNe IIn is presumably directly analogous. Nevertheless, the amount of kinetic energy that must be converted to radiation in order to accommodate these events requires an extremely massive circumstellar envelope and therefore a very large initial mass (Smith et al. 2010; Chatzopoulos et al. 2013), possibly within the range at which other evolutionary channels beyond ordinary core collapse may become relevant.

Events lacking narrow hydrogen lines (including all SLSNe I, but also any SLSNe II whose Balmer lines are broad and/or weak) represent an even greater challenge for progenitor models, since it is not clear whether interaction with a circumstellar medium is available to ease the radiative energy

requirements. It is possible that the ejecta are interacting with a dense, hydrogen-poor shell of previously ejected material (e.g., Chevalier & Irwin 2011; Ginzburg & Balberg 2012), although this would imply a very large initial mass and again point toward the possibility of exotic evolutionary or explosion channels. Furthermore, the absence of observed narrow lines from other elements is surprising. For SLSNe I, the stellar progenitor must also rid itself of its hydrogen envelope during its lifetime and yet retain sufficient mass at the time of death to produce an explosion with $E_K \approx 10^{51}$ erg ejecting $M_{\rm ej} \gtrsim 10\,M_\odot$ worth of heavy elements, a challenge for stellar evolutionary theory.

While it is possible that either or both classes of transient may simply constitute extrema of ordinary stellar evolution and explode via core collapse, the remarkable observational properties of SLSNe have sparked renewed interest in more exotic explosion mechanisms. One well-established model of particular theoretical interest is the pair-instability supernova (PISN), an explosion produced when the temperature required to maintain hydrostatic equilibrium in the core of a star becomes so high that photons disintegrate into particle pairs and the star collapses (Rakavy & Shaviv 1967; Barkat et al. 1967). Such events should originate from the most massive stars ($M_{\rm init} > 300\,M_\odot$; Yoshida & Umeda 2011) and are expected to produce enormous quantities of radioactive nickel that could easily power an SLSN; at least one well-known SLSN I (SN 2007bi) has been interpreted with reasonable success within this model (Gal-Yam et al. 2009; but see Dessart et al. 2012). In a variant on the pair-instability mechanism, the *pulsational* PISN, the massive star undergoes several incomplete pair-instability episodes, leading to a series of envelope-shedding eruptions before the final explosion (Woosley et al. 2007; Waldman 2008), naturally providing both an intrinsically very energetic explosion and shells of material for it to interact with. Problematically, however, classical pair-instability models lead to very large masses of ^{56}Ni; this decays to ^{56}Co, whose much slower decay to ^{56}Fe should produce a luminous exponential decay phase in the late-time light curve. While evolution consistent with this has been seen in a handful of cases (referred to as "Type R" SLSNe by Gal-Yam 2012), the majority fade too fast to be explained by this mechanism. High-mass, noninteracting core-collapse models (e.g., Yoshida et al. 2014) also share this problem.

Some, and perhaps all, SLSNe may therefore require yet another mechanism to reenergize the ejecta. If interaction and radioactive decay are excluded as possibilities, the only remaining power source capable of meeting the energy requirements is the compact object itself, the so-called "central engine." The most popular central-engine model invokes a spinning-down highly magnetic neutron star ("magnetar") that energizes the SN by winds and X-ray radiation from inside (Mazzali et al. 2006; Kasen & Bildsten 2010; Woosley 2010; Inserra et al. 2013; Metzger et al. 2015). Alternative central-engine models include jet feedback from fallback accretion onto the central neutron star or black hole (Gilkis et al. 2015; Soker 2016).

The host-galaxy environments of SLSNe provide strong constraints on progenitor models. For example, simple, single-star pair-instability models predict that PISNe should be produced only by stars with very low initial metallicity (Langer et al. 2007). If this model is correct, these explosions should not form in metal-rich environments. The energy-injection model involves a rapidly rotating central engine similar in nature to the central engine of gamma-ray bursts (GRBs; e.g., Usov 1992); if this model explains some or all SLSNe, then it would be reasonable to expect similarities between the hosts of SLSNe and the hosts of long-duration GRBs, which are observed to avoid high-metallicity galaxies and occur predominantly at low to intermediate metallicity in the local universe (Stanek et al. 2006; Modjaz et al. 2008; Graham & Fruchter 2013; Krühler et al. 2015; Japelj et al. 2016; Perley et al. 2016). Other models invoke dynamical interactions and stellar mergers in dense environments (Pan et al. 2012; van den Heuvel & Portegies Zwart 2013), which would favor particularly intense starbursts. In any case, regardless of the underlying theoretical model, the degree of similarity or dissimilarity between the hosts of Type I versus Type II events (or between subclasses of these events, or between these events and other classes of SNe) might help establish whether these explosions are closely related or fundamentally different.

The very fact that SLSNe were discovered only in the past decade provides evidence that the sites of SLSNe might differ from those of ordinary CCSNe. Prior to about 2005, all major nearby SN searches—most notably, the Lick Observatory Supernova Search (LOSS) with the Katzman Automatic Imaging Telescope (KAIT; Filippenko et al. 2001)—were targeted surveys, using small-field-of-view cameras to periodically image the positions of known galaxies. For reasons of efficiency, nearby and relatively high mass galaxies were preferentially targeted, rendering these searches insensitive to transients that might occur preferentially or exclusively in smaller systems (unless discovered in the background). However, starting about 10 yr ago, a number of wide-field untargeted optical surveys began operation, providing the capability to search much larger volumes of space in an unbiased manner; these include the Texas Supernova Search (which discovered the first widely recognized SLSNe, SN 2005ap and SN 2006gy), the Catalina Real-Time Survey (Drake et al. 2009), the Palomar Transient Factory (PTF; Law et al. 2009), Pan-STARRS (Kaiser et al. 2002), La Silla Quest (Hadjiyska et al. 2012), SkyMapper (Keller et al. 2007), the Dark Energy Survey (Dark Energy Survey Collaboration 2016), and the All-Sky Automated Survey for Supernovae (ASAS-SN; Shappee et al. 2014). A large fraction of the SLSNe reported by these surveys originate from very faint galaxies (Neill et al. 2011), undetected in pre-explosion images such as the Sloan Digital Sky Survey (SDSS). While in part this reflects the great distances at which SLSNe are discovered, more detailed analysis of SLSN host-galaxy samples suggests that they differ intrinsically from the host populations of more ordinary SNe in various ways: low masses and metallicities are typical (Chen et al. 2013; Lunnan et al. 2013, 2014; Angus et al. 2016), and galaxies with exceptionally strong emission lines are remarkably frequent (Leloudas et al. 2015).

Among these surveys, the PTF has been the most prolific discoverer of SLSNe: the sample of 32 SLSNe discovered in 2009–2012 that we present here (Section 2) is comparable in size to the sample of publicly released SLSNe from all other surveys combined. Furthermore, all of these events occurred at relatively low redshifts ($z < 0.51$), so in all cases the SN and host are relatively accessible to comprehensive follow-up observations. In contrast, Pan-STARRS, the next most prolific individual survey with a published SLSN sample, has

discovered most of its SLSNe at significantly greater distances ($0.5 < z < 1.6$ from the sample of Lunnan et al. 2014).

In complementary papers we will be presenting the entire suite of observations of the PTF SLSN sample, including details of the discovery and sample selection, spectroscopic properties (Leloudas et al. 2016; R. Quimby et al. 2016, in preparation), and multiband light curves (A. De Cia et al. 2016, in preparation). In this work we present observations of the host galaxies of these events from an extensive ground- and space-based campaign, effectively doubling the sample of well-studied SLSN hosts and providing the first large, homogeneous, single-survey sample in the local universe.

The paper is organized as follows. In Section 2 we overview the operations in PTF leading to successful discovery and classification of SLSNe and outline the selection of our sample. Our observations are described in Section 3, including ultraviolet (UV), optical, and near-infrared (NIR) photometry and spectroscopy from Keck and Palomar supplemented by *Hubble Space Telescope (HST)* and *Spitzer* imaging; we also summarize our analysis techniques used to provide measurements of physical parameters such as mass, star formation rate (SFR), and metallicity using these observations. The host galaxies are discussed on an individual basis in Section 4. In Section 5 we examine our SLSN sample as an ensemble and compare the physical properties of the population against those of volume-limited star-forming field-galaxy samples. We discuss our results and their implications in Sections 6 and 7.

2. SAMPLE SELECTION

2.1. PTF Discovery of Supernovae

The current public literature sample of SLSNe and SLSN hosts (see, e.g., Leloudas et al. 2015; Angus et al. 2016) is combined from a large variety of different surveys, each of which contributes only a few events to the overall total.[11] Many of these discoveries were based on archival reanalysis of earlier surveys (such as SDSS; Leloudas et al. 2012) to recover events that were not recognized to be SLSNe at the time. Consequently, the existing sample of low-z SLSNe is quite heterogeneous in construction, and the biases that may affect the nature of the cataloged population are nontrivial. In contrast, the PTF sample we present here was discovered by a single survey using a single camera and telescope and via (typically) the same group of scientists and follow-up resources. Nevertheless, PTF is a complex effort, and its cadence, motivations, and emphasis have varied substantially since its inception, so the sample presented here is subject to its own biases and incompletenesses. Discussion of possible biases related to these factors will be presented in Section 6.1. We provide a brief summary of the survey and its operations below.

The PTF is a synoptic optical survey using the 48-inch Oschin Schmidt Telescope (P48) at the Palomar Observatory near San Diego, California, and a 7.2 deg^2 camera (Rahmer et al. 2008). Observations of the sky are acquired every night during clear weather, except within a few days of full moon each month when Hα survey observations are performed. PTF operated between 2009 and 2012, and although the facility is continuing operations as the intermediate Palomar Transient

Factory (iPTF) until the end of 2016, this paper exclusively addresses events discovered during the original 4 yr period. PTF employs both R- and g-band filters, but prior to 2013 the large majority of the survey was conducted in R, and all of the SLSNe presented here were discovered in R.

The survey discovers far more transient events than can be observed spectroscopically: the PTF database reports 19,595 likely transients discovered in 2009–2012, of which only 2131 (11%) have secure classifications. Human oversight is necessary at several stages in the process to choose astrophysically real and scientifically interesting targets for follow-up observations. All objects found by the automated detection and verification pipelines (Brink et al. 2013) are screened by human scanners to confirm their astrophysical nature and rule out nontransient false positives (cosmic rays, poor subtractions, asteroids, and variable sources). At the time of discovery, the scanner may choose to nominate an object for follow-up spectroscopy. Objects may also be nominated later, as further data are collected. Weather permitting, these are then targeted at the next observing run (usually 1–2 runs occur monthly during dark time). Spectra are reduced within a few days of being acquired, and a preliminary classification is established either visually or via standard classification routines; events with unclear or ambiguous classifications are flagged for reobservation with higher signal-to-noise ratio (S/N) or at later epochs. Classifications are revisited at later times once all data are in hand.

2.2. Definition and Identification of SLSNe

The class of SLSNe is necessarily defined via a combination of photometric and spectroscopic qualities: to qualify, an event must be clearly an SN (usually implying the detection of broad features in the spectrum, as well as an SN-like light curve and color evolution) and also must be much more luminous than ordinary SNe (it must be "super" luminous). Beyond this there is no standard definition of what observables are required to establish what is or is not an SLSN. An absolute magnitude limit of $M < -21$ at peak was adopted by Gal-Yam (2012), but this choice is empirical and somewhat arbitrary (it is also wavelength dependent). Furthermore, several SNe with properties very similar to those of SLSNe I in particular (in terms of colors, light curves, spectra, and total radiative output) do not quite reach this luminosity, while a small number of SNe that are probably not related to massive stars at all (specifically the Type Ia-CSM SNe; Silverman et al. 2013) occasionally do surpass it.

The task of defining SLSNe in a physically meaningful way, as well as the isolation of all events within PTF satisfying that definition, is therefore quite complicated. A detailed analysis of this topic will be deferred to the upcoming dedicated works of R. Quimby et al. (2016, in preparation), A. De Cia et al. (2016, in preparation), and G. Leloudas et al. (2016, in preparation) including a presentation of all spectra and light curves. For the purposes of this paper, we establish our own working definition of SLSNe in the PTF sample as follows.

We require, at minimum, an absolute magnitude of $M_R < -20.0$ at peak to consider inclusion of an event in our sample. This guarantees that every event in our sample is indeed very luminous and eliminates the vast majority of ordinary SNe in the PTF sample. Circumstellar interaction is capable of significantly boosting the luminosity of all types of SNe (Ofek et al. 2014); indeed, SNe IIn have in particular been known since the 1980s to exceed this threshold on occasion

---

[11] The relatively large Pan-STARRS sample of 15 events presented by McCrum et al. (2015) and Lunnan et al. (2014) is an exception, but it probes a higher and more difficult-to-study redshift range.

(Richardson et al. 2002). We therefore apply a more stringent cut if narrow hydrogen lines are present, requiring $M_R < -20.5$ at peak. (A few events were discovered after peak brightness, and one is heavily extinguished by host-galaxy dust. In these cases peak magnitudes require extrapolations or corrections; see Section 2.4.)

Many of the most luminous transient candidates identified by PTF turn out to not be SNe: active galactic nuclei (AGNs) and quasi-stellar objects (QSOs) are particularly common. Most such objects can be easily eliminated from consideration based on their past or continued variability or via spectroscopy; alternatively, an off-nuclear location or a smoothly rising and falling light curve with blue-to-red spectral evolution usually provides good evidence that a transient is an SN and not an AGN. Even so, SLSNe II can look spectroscopically similar at certain phases to narrow-line AGNs (as can normal SNe IIn; e.g., Filippenko 1989), and in cases where photometric and spectroscopic coverage of the SN is poor it is not always easy to completely rule out an AGN flare. For two events in our sample (PTF 09uy and PTF 11dsf), we favor an SLSN interpretation but note that an AGN has not been fully eliminated (see also the discussion of PTF 10tpz in Section 6.3). These classifications will be further investigated and discussed by G. Leloudas et al. (2016, in preparation).

Tidal disruption events (TDEs) represent another, less frequently observed class of phenomena associated with accretion onto supermassive black holes. These typically exhibit peak magnitudes around -19 but can occasionally be brighter than -20 (Arcavi et al. 2014). The spectroscopic and photometric properties of TDEs and SLSNe are usually distinct —and while ambiguous cases can arise especially at the high-luminosity end (Chornock et al. 2014; Leloudas et al. 2017; G. Duggan et al. 2016, in preparation; see also the last paragraph of Section 7), these are particularly rare, and we identify no such cases within the 4 yr PTF sample covered here.

The most luminous SNe Ia exceed -20 mag but are easily identified spectroscopically. Type Ia-CSM SNe can be even brighter (occasionally, even < -21 mag), but as photospheric SN Ia features are still evident, these can similarly be identified spectroscopically (Silverman et al. 2013). In the course of this analysis we identified several new SNe Ia-CSM within the PTF sample that will be reported in separate work.

Other types of luminous transients are also known to exist whose connection to SNe is not yet clear, in particular the fast-rising transients of Arcavi et al. (2016) and Drout et al. (2014). With the exception of the single event already identified by Arcavi et al. (2016), we find no further members of these classes in our sample.

In total, 32 events satisfy all of the above criteria and constitute the PTF SLSN sample. All show behavior characteristic of SNe, including broad spectral lines, evolutionary timescales of months, and blue-to-red spectral evolution in cases where multiband data are available.

2.3. Subclassification of SLSNe

SLSNe within the sample are then subcategorized spectroscopically as Type "I" or "II" based on the absence or presence (respectively) of hydrogen in their spectra. While in principle this is a straightforward distinction, it conceals some complexity. For example, a few SLSNe show no hydrogen in any of their early-time spectra but then develop broad hydrogen lines

at late times (Gezari et al. 2009; Miller et al. 2009; Benetti et al. 2014; Yan et al. 2015). Even for events that do exhibit hydrogen emission in all existing spectra, this emission can sometimes be relatively weak and/or exhibit no narrow component. While a strictly literal interpretation would classify these events as Type II, some of them may quite plausibly be physically more closely related to SNe I (or represent an intermediate case or another class entirely; see also Inserra et al. 2016).

In spite of these occasional ambiguities, the "I" versus "II" distinction is sufficient for the vast majority of events in our sample: nearly all events without hydrogen at the time of discovery never show hydrogen in any follow-up spectra, and nearly all events with hydrogen exhibit strong emission lines at all phases including a narrow component. The possible exceptions include PTF 10aagc (Type I with ambiguous, weak, late-time broad hydrogen), PTF 10uhf (Type I, but with a possible faint signature of broad Balmer emission that is difficult to disentangle from the host [N II] emission), and PTF 12gwu (Type II, but the hydrogen lines are much weaker than in the rest of our sample and no obvious narrow component is present). For this paper, we maintain the initial, conservative classifications of these events from the presence or absence of unambiguous hydrogen in their discovery spectra.

Among the SLSNe I, we denote a small number of events (three) as belonging to the subclass of long-lived "R"-types, which show exponentially declining late-time light curves consistent with radioactive decay and which have been suggested to be examples of PISNe (Gal-Yam et al. 2009; Gal-Yam 2012), although this interpretation is contested by other authors (e.g., Dessart et al. 2012; Nicholl et al. 2013; Jerkstrand et al. 2016). We will generally refer to them as Type "I-R." With only three events, we do not have sufficient sample size to perform a statistically robust comparison between the host properties of these events and the more rapidly declining SNe I, but as we observe no strong distinction between the host properties of these events and other SLSNe I in our sample (and other authors have reported similar results; e.g., Lunnan et al. 2014; Leloudas et al. 2015), we will generally treat all SLSNe I together in our analysis regardless of their light-curve properties.

2.4. Sample Properties

The sample is summarized in Table 1. In total, we present 14 events of Type II and 18 events of Type I, only three of the latter being Type R. The large majority of these objects have not been previously presented in the literature.

Two of the SLSNe are noteworthy from the point of view of sample selection. PTF 10vwg is in a crowded low-Galactic-latitude field and, while detected in PTF survey images, was not identified as a transient candidate until it was discovered in the background of an LOSS/KAIT image (Kodros et al. 2010) —so it is not truly a PTF object. (Stellar confusion and high foreground extinction also introduce severe complications in characterizing the host.) PTF 10tpz is near the nucleus of an early-type galaxy, and the SN spectrum is highly reddened owing to host extinction. Without an extinction correction it would not be superluminous, but depending on the (highly uncertain) host column, it is probably close to or above our threshold. Were it not for the known example of SN 2006gy, which occurred under similar circumstances (e.g., Ofek et al. 2007; Smith et al. 2007), this event would likely not have been

<div align="center">

Table 1
Superluminous Supernovae from PTF

</div>

PTF ID	α[a]	δ[a]	Class[b]	z	$M_{V,\text{peak}}$[c]	t_{peak}[c]	E_{B-V}[d]	Notes
09as	12:59:15.864	+27:16:40.58	I	0.1867	−20.8	2009 Mar 24	0.008	⋯
09uy	12:43:55.771	+74:41:07.58	II	0.3145	−21.2	2009 Jul 08	0.020	⋯
09atu	16:30:24.553	+23:38:25.43	I	0.5015	−22.5	2009 Aug 18	0.042	⋯
09cnd	16:12:08.839	+51:29:16.01	I	0.2584	−23	2009 Sep 10	0.021	⋯
09cwl	14:49:10.08	+29:25:11.4	I	0.3499	−22.5	2009 Sep 07	0.014	=SN 2009jh
10bfz	12:54:41.288	+15:24:17.08	I	0.1701	−20.9	2010 Jan 31	0.018	⋯
10bjp	10:06:34.30	+67:59:19.0	I	0.3584	−21.4	2010 Feb 16	0.055	⋯
10cwr	11:25:46.73	−08:49:41.9	I	0.2297	−21.8	2010 Mar 21	0.035	=SN 2010gx
10fel	16:27:31.103	+51:21:43.45	II	0.2356	$<$−20.5	$<$2010 Apr 03	0.017	⋯
10heh	12:48:52.05	+13:26:24.5	II	0.3379	−21.2	2010 Jun 03	0.024	⋯
10hgi	16:37:47.074	+06:12:31.83	I	0.0987	−20.3	2010 Jun 20	0.074	=SN 2010md
10jwd	16:43:43.325	+44:31:43.8	II	0.477	−21.4	2010 Jul 02	0.012	⋯
10nmn	15:50:02.809	−07:24:42.38	I-R	0.1237	−20.5	2010 Jul 07	0.138	⋯
10qaf	23:35:42.887	+10:46:32.57	II	0.2836	−21.6	2010 Aug 05	0.070	⋯
10qwu	16:51:10.572	+28:18:07.62	II	0.2258	−21.0	2010 Aug 21	0.040	⋯
10scc	23:28:10.495	+28:38:31.10	II	0.242	−21.5	2010 Aug 26	0.093	⋯
10tpz	21:58:31.74	−15:33:02.6	II	0.0395	$\ll$−19	2010 Sep 02	0.041	Heavily extinguished
10uhf	16:52:46.696	+47:36:21.76	I	0.2882	−22	2010 Sep 18	0.018	Possible very weak Hα?
10vqv	03:03:06.859	−01:32:35.42	I	0.4518	−22.5	2010 Oct 13	0.061	⋯
10vwg	18:59:32.881	+19:24:25.74	I-R	0.1901	−21	2010 Sep 07	0.467	=SN 2010hy; KAIT/LOSS discovery
10yyc	04:39:17.297	−00:20:54.5	II	0.2147	−21	2010 Nov 13	0.041	⋯
10aagc	09:39:56.923	+21:43:17.09	I	0.206	−20.4	2010 Oct 04	0.022	Late-time hydrogen lines?
11dij	13:50:57.798	+26:16:42.44	I	0.1428	−21.5	2011 Apr 28	0.011	=SN 2011ke
11dsf	16:11:33.55	+40:18:03.5	II	0.3848	−22.1	2011 May 27	0.009	⋯
11hrq	00:51:47.22	−26:25:10.0	I	0.057	$<$−20	$<$2011 Jul 11	0.012	⋯
11rks	01:39:45.528	+29:55:27.43	I	0.1924	−21.1	2012 Jan 11	0.038	⋯
12dam	14:24:46.228	+46:13:48.64	I-R	0.1073	−21.5	2012 Jun 12	0.100	⋯
12epg	12:55:36.596	+35:37:35.79	II	0.3422	−21.3	2012 May 30	0.015	⋯
12gwu	15:02:32.876	+08:03:49.47	II	0.275	−21.4	2012 Jul 25	0.033	Hydrogen lines very weak
12mkp	08:28:35.092	+65:10:55.60	II	0.153	−21.0	2013 Jan 25	0.046	⋯
12mue	03:18:51.072	−11:49:13.55	II	0.2787	−21.4	2012 Dec 21	0.062	⋯
12mxx	22:30:16.728	+27:58:22.01	I	0.3296	−22.5	2012 Dec 10	0.041	⋯

Notes.
[a] Supernova position (J2000).
[b] Supernova classification.
[c] Approximate peak visual magnitude of the supernova and corresponding UT date. More refined measurements will be presented by A. De Cia et al. (2016, in preparation).
[d] Galactic (foreground) selective extinction in magnitudes; from Schlafly & Finkbeiner (2011).

(This table is available in machine-readable form.)

categorized as an SLSN. In any case, the considerations involving its discovery are quite different than for other PTF events (a much smaller effective detection volume because of the large extinction, plus more complex issues involving host subtraction and AGN contamination), so it should not be treated with statistical weight equal to the others. We will include the hosts of these events in our plots and analysis where possible, but we emphasize that they would be excluded from any attempt to produce a statistically uniform sample from these data.

3. OBSERVATIONS

3.1. Ground-based Imaging

The SLSNe in the sample above were targeted for late-time imaging in a variety of wavebands spanning the near-UV to the NIR. Several host galaxies were bright enough to be well recovered in SDSS (at least in the *gri* filters), so we downloaded the processed survey images from the SDSS archive (Alam et al. 2015). For fainter hosts and for other filters

we observed with other facilities: the Palomar 60-inch (P60) telescope imaging camera (Cenko et al. 2006), the Large Format Camera or the Wide-Field Infrared Camera (WIRC) on the Palomar 5-m Hale telescope, or the Low-Resolution Imaging Spectrometer (LRIS; Oke et al. 1995) or the Multi-Object Spectrometer for Infrared Exploration (MOSFIRE; McLean et al. 2012) on the Keck I 10 m telescope.

All ground-based images used for the host-galaxy spectral energy distribution (SED) analysis were acquired either pre-explosion or long after the SN peak time (at least 2 yr, typically 3–4 yr). Nevertheless, SLSNe exhibit a range of light-curve behaviors and decay times, and there is no guarantee based on the time difference alone that the SN is not contributing light. We use various checks appropriate to the situation to rule out significant SN contributions: (1) direct confirmation based on a reference-subtracted image that the SN was much fainter than the host well prior to the observation in question, (2) verifying nonvariability between widely spaced epochs, (3) absence of any SN-like broad features in high-S/N contemporaneous (or earlier) spectra, or detection of features whose contribution to

the overall flux is negligible, and (4) a clearly resolved host with no pointlike component visible at the SN location.

Observations were reduced via standard procedures (our own tools were developed and used for the reduction of LRIS, MOSFIRE, and WIRC data). We localized the SN position by comparison to images taken with the P60 at early times while it was bright, though in a handful of cases no P60 imaging was available and we used the P48 survey images instead. In nearly all cases we identify a host galaxy directly underlying this location at late times. For a few objects the nearest well-detected source is somewhat offset from the SN position, or there is ambiguity regarding whether sources in the image constitute a single galaxy or multiple galaxies; we will discuss these cases individually in Section 4.

Once the host is identified, we measure its centroid and perform aperture photometry using our own IDL tools, setting the aperture radius for each galaxy to be sufficiently large as to include all of the host flux. The same aperture radius is used for all filters. In one case (PTF 11dij) a neighboring galaxy unavoidably contaminates the host position in all ground-based images; we modeled and subtracted it with GALFIT (Peng et al. 2002) before performing photometry on the subtracted images. The photometric calibration scale is established either by direct comparison to SDSS or to the Two Micron All Sky Survey (2MASS; Cohen et al. 2013) or (for optical fields outside SDSS) from a field calibration of secondary standards gathered using the P60 on photometric nights. We omit photometry that results only in shallow upper limits that do not usefully constrain the SED models. We also omit a few points from the literature that are inconsistent with our own photometric measurements in the same or similar bands at high significance.

Thumbnail images of all our fields are presented in Figure 1. Final photometry, including supplementary observations from the literature (Lunnan et al. 2015; Angus et al. 2016), is presented in Table 2 and displayed in Figure 2. We report both magnitudes (in the default calibration system of the relevant filter and uncorrected for foreground extinction) and extinction-corrected fluxes (using the dust maps of Schlafly & Finkbeiner 2011).

3.2. HST Observations

Several host galaxies of slowly declining (Type I-R) hydrogen-poor SLSNe were observed with *HST* as part of our team's approved programs (GO-12983, PI O. Yaron; GO-13858, PI A. De Cia). PTF 10nmn was observed with the Advanced Camera for Surveys (ACS) in the Wide Field Channel through the F625W filter, while PTF 12dam and PTF 11hrq were observed with the Wide Field Camera 3 (WFC3) in the Ultraviolet-Visible (UVIS) channel using filters F625W, F336W, and F225W.

For the ACS observations, reduced images of the separate exposures were produced by the ACS data calibration pipeline (CALACS), which includes a correction for the bias striping and cross-talk effects and the charge transfer efficiency (CTE). For the UVIS observations, we corrected for the CTE using the `ctereverse` FORTRAN routine provided[12] by the Space Telescope Science Institute (STScI). After cosmic-ray removal using the LA Cosmic routine of van Dokkum (2001), we astrodrizzled the reduced frames to a final image with

DrizzlePac 2.0[13] with inverse variance map weighting, adopting a pixel size of 0″033. If only two images were available (for the PTF 11hrq and PTF 12dam UVIS observations), we adopted a pixel fraction of unity in the drizzling, while for the others we used a pixel fraction 0.6.

The host-galaxy magnitudes were determined using circular aperture photometry, using zero points from the ACS and WFC3 handbook and applying an aperture correction to an infinite aperture.

Some of our *HST* observations were conducted within 1–2 yr after the SN in order to follow the late-time evolution of the light curve, and the SN is still clearly detected. For the PTF 10nmn observation, the SN is well offset from the bulk of the host-galaxy light; we subtracted the SN contribution by PSF fitting of the SN using the profile of a nearby star on the same final image with a custom IDL routine. For PTF 11hrq, the SN location is also offset from the host galaxy, but it is not clearly detected in the *HST* image, and no correction is applied. For PTF 12dam, it is difficult to directly estimate the SN brightness as its location is consistent with a compact but resolved knot of the host galaxy; however, its contribution (relative to the host) is negligible in roughly coeval ground-based photometric and spectroscopic observations.

Additional UV and NIR observations of various events in the sample (PTF 09atu, PTF 09cnd, PTF 09cwl, PTF 11dij, PTF 11dsf, PTF 11rks) were obtained as part of programs GO-13025 and GO-13480 (PI A. Levan). Photometry is taken directly from the recent publication of Angus et al. (2016) with the exception of the F160W photometry of PTF 11rks, which we recalculated using a larger aperture, which is more appropriate given the diffuse extensions apparent in the ground-based optical imaging. All *HST* photometry is presented alongside our ground-based measurements in Table 2 and Figure 2.

3.3. Spitzer and Wide-field Infrared Survey Explorer (WISE) Observations

Several host galaxies in our sample were observed with IRAC on the *Spitzer Space Telescope* during Cycle 10 (GO-10056, PI R. Lunnan). Sources were observed in channel 1 ($\lambda = 3.6\ \mu$m) using a frame time of 100 s per exposure. A total integration time of 3600 s was used for each of PTF 09cnd, PTF 09atu, and PTF 09cwl; 1800 s was used for PTF 10cwr, PTF 10hgi, and PTF 11dij; and 1200 s was used for PTF 11rks and PTF 12dam. We downloaded the processed (PBCD) images from the *Spitzer* Heritage Archive, subtracted all nearby contaminating sources, and performed aperture photometry on the host galaxy using the procedure outlined by Perley et al. (2016). Photometry is presented in Table 2.

Many of our galaxies are sufficiently bright to be detected in archival data from *WISE* (Wright et al. 2010). We downloaded photometry from the online catalogs of the ALLWISE Data Release (Cutri et al. 2013)[14] and include them in our tables and SED fits.

3.4. Spectroscopy

Spectra were obtained for most host galaxies within the sample using LRIS on the Keck I telescope. We used the 400/8000 grating on the red side and either the 400/3400 or 600/
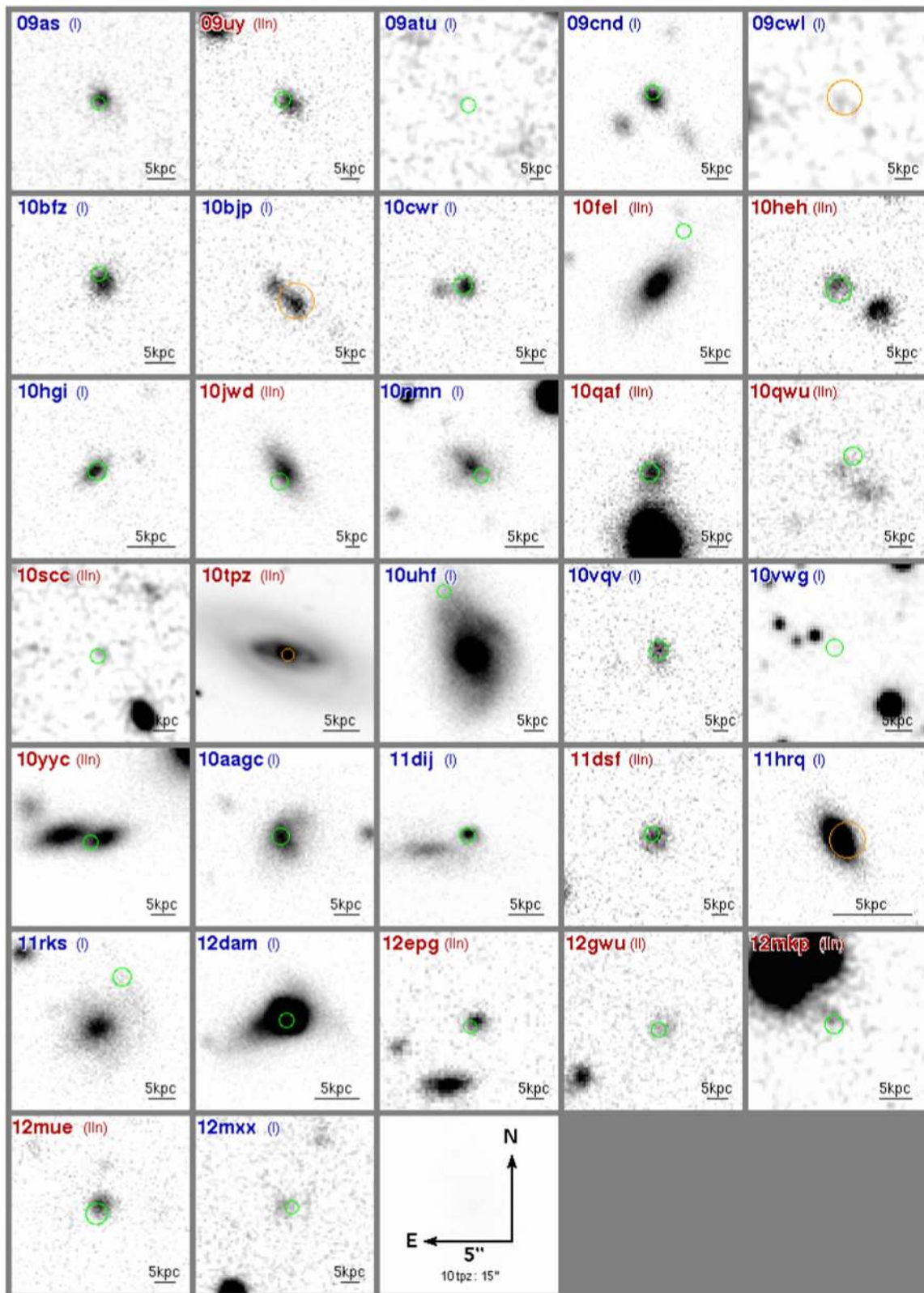

Figure 1. Mosaic showing ground-based images of 32 PTF SLSN host galaxies from Keck and Palomar (*R*- or *I*-band images except for PTF 10vwg and PTF 12epg, where we display *J*-band images, and PTF 09as, where we display a *u*-band image). Images are $10''$ on each side, except for the image of PTF 10tpz ($30''$). The host population exhibits a wide variety of morphologies, sizes, and luminosities, although mergers/companions are very common, and massive spirals are largely (but not entirely) deficient. Circles show the SN position, with the radius denoting the approximate uncertainty (green circles indicate positions from the P60 follow-up telescope; orange circles are from the P48 survey telescope).

Table 2
Photometry of SLSN Hosts

PTF ID	Filter	Magnitude[a]	F_ν[b]	Date	Instrument	Reference
09as	u	23.01 ± 0.06	2.25 ± 0.13	2016 Jun 07	KeckI/LRIS	This work
	g	22.35 ± 0.10	4.28 ± 0.41	2004 Dec 21	SDSS	This work
	r	21.73 ± 0.09	7.53 ± 0.65	2004 Dec 21	SDSS	This work
	i	21.71 ± 0.14	7.63 ± 1.05	2004 Dec 21	SDSS	This work
	z	21.20 ± 0.36	12.43 ± 4.89	2004 Dec 21	SDSS	This work
09uy	u	24.18 ± 0.16	0.81 ± 0.13	2016 Jun 07	KeckI/LRIS	This work
	B	23.92 ± 0.05	1.20 ± 0.06	2013 Apr 09	KeckI/LRIS	This work
	R	22.53 ± 0.05	3.16 ± 0.15	2013 Apr 09	KeckI/LRIS	This work
	z	22.40 ± 0.08	4.18 ± 0.32	2016 Jun 07	KeckI/LRIS	This work
	J	21.34 ± 0.13	4.71 ± 0.60	2014 Jun 15	KeckI/MOSFIRE	This work
	Ks	20.37 ± 0.19	4.77 ± 0.91	2014 Jun 15	KeckI/MOSFIRE	This work

Notes.

[a] Magnitudes are expressed in the conventional frame for each relevant filter: specifically, SDSS filters (*ugriz*) are reported in the SDSS system, while Johnson-Cousins filters (*BVRI*) are reported in Vega magnitudes. NIR filters (*JHK_s*) are reported in the 2MASS system. Space-based (*HST/Spitzer/WISE*) magnitudes are AB (Oke & Gunn 1983). Magnitudes are not corrected for foreground extinction.
[b] Flux densities in μJy (calculated from our standard magnitudes via Fukugita et al. 1995), corrected for foreground extinction.

(This table is available in its entirety in machine-readable form.)

4000 grism on the blue side, providing continuous coverage between the near-UV and 10300 Å. In cases where our ground-based imaging was able to clearly resolve the host, the slit was aligned with the major axis of the galaxy to minimize slit losses (in all cases a 1″ slit was used); otherwise, the parallactic angle (Filippenko 1982) was used. LRIS is equipped with an atmospheric dispersion corrector (Phillips et al. 2006), so flux losses associated with nonparallactic angles are minimal. A few systems (PTF 10uhf, PTF 10tpz, PTF 11rks) exhibit large, resolved hosts that cannot be easily accommodated in the slit; both of these systems appear to be special cases and are discussed individually later. A log of all exposures is presented in Table 3.

All LRIS spectra were reduced in a standard manner using the tools in our custom LRIS pipeline LPipe,[15] with the extraction aperture carefully determined to include all nebular flux from the host galaxy evident in the two-dimensional frames and exclude flux from neighboring companion objects.

Two host galaxies were observed with DEIMOS (Faber et al. 2003) on the Keck II telescope at the parallactic angle: PTF 10hgi and PTF 12epg. The data were reduced within IRAF using a similar general procedure as the LRIS data.

Flux calibration was performed relative to standard stars using the same setup and (where possible) similar airmass. The portions of the LRIS spectra separated by the blue and red cameras were joined with the flux rescaled based on the measured source plus sky flux within the aperture. We note that this process (based on a relatively small overlap region over which the transmission on both sides varies rapidly with wavelength) produces some additional systematic uncertainties in comparing relative fluxes in the blue versus the red halves of the spectra, particularly for sources observed with the 600/4000 grism (which affords limited wavelength overlap). For sources with measurable continuum, absolute flux calibration (including correction for slit losses) is performed by calculating synthetic photometry on the reduced spectrum and scaling relative to our photometric measurements. For many of our targets there is no measurable host continuum or the uncertainty in the continuum flux level is dominated by the

sky-continuum background subtraction, so the spectroscopic flux calibration is used directly with no rescaling.

The DEIMOS spectrum of PTF 10hgi was obtained only 1 yr after the SN and contains significant SN light; in this case, we calibrate the fluxes by scaling the spectrum to match the Hα flux of this object as presented by Leloudas et al. (2015). We also take the [O II] flux from Leloudas et al. (2015), since this line is not covered by the wavelength range of this DEIMOS spectrum. All other spectra were obtained sufficiently late that the SN was not a significant source of emission.

Our spectra are plotted in Figures 3–5 and have been uploaded to WiseREP[16] (Yaron & Gal-Yam 2012).

3.5. SED Fitting

To estimate the stellar parameters of the host galaxies (M_*, SFR, and A_V), we analyze the UV–optical–NIR SEDs using a custom SED-fitting code (previously developed by D. Perley and used in, e.g., Perley et al. 2013). The code uses the population-synthesis templates of Bruzual & Charlot (2003) summed according to a parametric star formation history. We assume a Chabrier (2003) initial mass function (IMF) and a stellar metallicity set between 0.2 and 1.0 solar—using our best estimate from the spectroscopic analysis where possible, or otherwise estimated from the mass–metallicity relation (see Section 5.6) after an initial fit to measure the stellar mass M_*. The contribution of nebular lines to the photometry is included, with the line parameters also fixed using the spectroscopic analysis (see next section). The star formation history of each galaxy is fit as a two-population model, with the maximum age of the older population fixed to the age of the universe at the redshift of the host, and the maximum age of the younger population free (but required to be at least 10 Myr). Both populations are assumed to have a continuous star formation history from the maximum age until today, so the overall star formation history is constant with an abrupt increase at an arbitrary time t_{burst}, the age of the current ongoing starburst. Dust attenuation is assumed to follow the Calzetti et al. (2000) template.
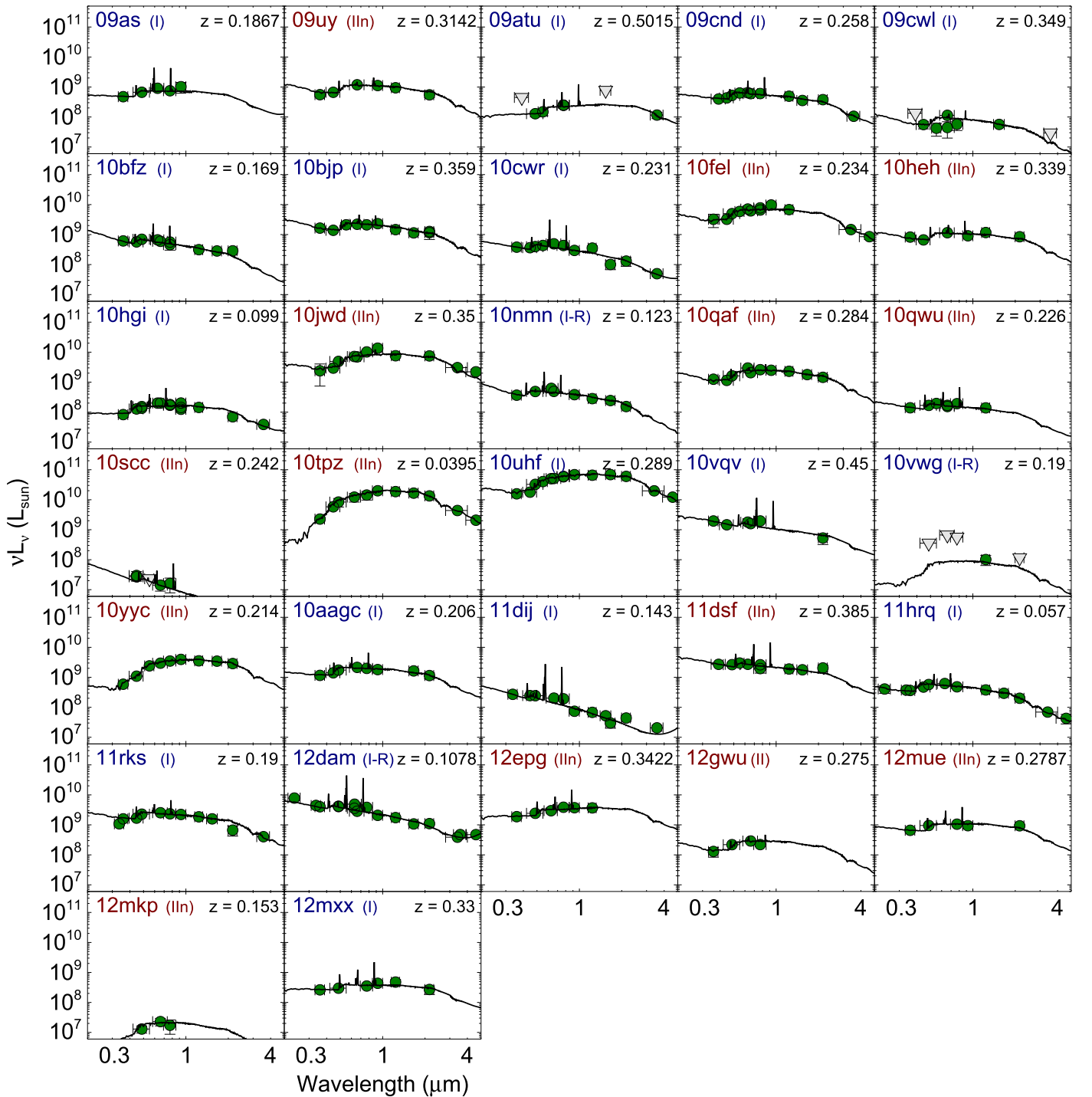
Figure 2. Spectral luminosity distributions for the host galaxies of all SLSNe in PTF, showing our multiband photometry (green circles) and best-fit SED model using the procedure outlined in 3.5. The scale of every subplot is identical, although note that the abscissa is in the observer frame and the ordinate shows the νL_ν luminosity. Gray triangles indicate upper limits.

For a few host galaxies, we do not have sufficient data to constrain all parameters in the model. In these cases we fix the burst age to 100 Myr (this is approximately the timescale to which near-UV luminosities are sensitive, and it enables a reasonable estimate of the average SFR) and/or the extinction A_V to zero, to enable us to still fit the data and obtain reasonable estimates of the SFR and M_*. We also fix the burst age to 100 Myr if the SED fit converged to a "negative" burst corresponding to a decrease in SFR in the recent past. We

apply a continuous star formation history in cases where the fit permitting an impulsive change converges to a result indistinguishable from this model.

Our results are presented in Figure 2 and Table 4.

3.6. Spectroscopic Analysis

To measure emission-line fluxes from our one-dimensional spectra, we first subtract the host continuum from the SED model (Section 3.5) convolved to the resolution of the spectra

Table 3
Log of Spectroscopic Observations

PTF ID	Obs. Date	Setup[a]	Exposure[b]	PA[c]
09as	2016 Jan 12	400/3400, 400/8500	2 × 900, 2 × 900	235
09uy	2014 Apr 30	400/3400, 400/8500	1300, 2 × 600	44
09atu	2014 Apr 29	600/4000, 400/8500	1140, 1140	5
09cnd	2014 May 28	400/3400, 400/8500	3 × 503, 3 × 500	308.5
09cwl	2014 Apr 29	600/5000, 400/8500	1000	171.5
	2014 May 28	400/3400, 400/8500	3 × 803, 3 × 800	171.5
10bfz	2015 Apr 23	400/3400, 400/8500	2 × 600, 2 × 600	285
10bjp	2013 Dec 04	600/4000, 400/8500	600 + 700, 2 × 600	222
10cwr	2014 Nov 29	400/3400, 400/8500	930, 900	307.7
10fel	2014 May 27	400/3400, 400/8500	1200, 2 × 500	31
10heh	2014 Apr 29	600/4000, 400/8500	900 + 2 × 970, 3 × 900	240.5
10hgi	2011 Jun 01[d]	DEIMOS 600ZD	3 × 1200 + 900	62
10jwd	2014 Apr 29	600/4000, 400/8500	2 × 600, 2 × 600	33
10nmn	2014 Apr 29	300/5000, 400/8500	1300 + 2 × 1200, 900 + 1150 + 1130	47
10qaf	2013 Oct 06	600/4000, 400/8500	1360, 2 × 600	183
10qwu	2014 May 28	400/3400, 400/8500	2 × 603, 2 × 600	314
	2014 Jul 31	400/3400, 400/8500	1200, 2 × 600	130
10scc	2014 May 28	400/3400, 400/8500	803 + 733, 700 + 660	274
10tpz	2016 Jun 06	400/3400, 400/8500	530 + 550, 2 × 500	70
10uhf	2013 Oct 06	600/4000, 400/8500	720, 700	199
			1320, 2 × 600	225
10vqv	2013 Oct 06	600/4000, 400/8500	2000, 2 × 900	181
10vwg	2013 Oct 06	600/4000, 400/8500	720, 700	86.5
10yyc	2013 Dec 04	600/4000, 400/8500	1130, 2 × 500	90
10aagc	2013 Dec 02	400/3400, 400/8500	1300, 2 × 600	0
11dij	2014 Apr 29	600/4000, 400/8500	1100, 2 × 500	110
11dsf	2014 Apr 29	600/4000, 400/8500	600 + 540, 600 + 500	0
11hrq	2013 Oct 06	600/4000, 400/8500	1360, 2 × 600	210
11rks	2012 Jul 15	400/3400, 400/8500	2 × 1800 + 900, 5 × 850	338[e]
	2013 Oct 06	600/4000, 400/8500	2000, 2 × 900	207
	2013 Dec 04	600/4000, 400/8500	900, 900	207
12dam	2014 Apr 29	600/4000, 400/8500	1200, 1200	286.9
	2014 Apr 30	400/3400, 400/8500	2 × 1000, 2 × 100	286.9
12epg	2016 Jan 06	DEIMOS 600ZD	3 × 1200	74
12gwu	2013 May 09[d]	400/3400, 400/8500	2 × 900, 2 × 870	323
12mkp	2015 Jan 22[d]	400/3400, 400/8500	2 × 900	170
12mue	2014 Sep 23	400/3400, 400/8500	2 × 600, 2 × 600	9
12mxx	2014 Aug 31	400/3400, 400/8500	600, 590	250
	2014 Sep 23	400/3400, 400/8500	900 + 1900, 3 × 900	104

Notes.
[a] LRIS-B grism and LRIS-R grating, unless another instrument is specified.
[b] Exposure sequence (seconds per exposure). Comma denotes separate sequences for LRIS-B and LRIS-R.
[c] Sky position angle used for the slit, in degrees. (Zero = north up, with a positive angle indicating rotation counterclockwise on the sky.)
[d] Spectrum contains significant SN contribution.
[e] Slit centered on the SN and not aligned with the host nucleus.

(This table is available in machine-readable form.)

to remove stellar Balmer absorption, and then we fit a Gaussian to the profile of all lines of interest (Hα, Hβ, Hγ, [O II] λ3727, [O III] λλ4363, 4959, 5007, [N II]λλ6548, 6583, [S II] λλ6716, 6731). For faint lines, the width and velocity center of the line model are tied to a nearby strong line: e.g., [N II] is tied to Hα. The components of the [O II] doublet are always blended at the resolution of our spectra and are reported as a total flux. These fluxes are given in Table 5. Equivalent widths are calculated at the same time using the measured (pre-subtraction) continuum.

A variety of standard techniques are then used to measure several key physical parameters associated with the fluxes and ratios of nebular lines for each host. All lines are first corrected for foreground extinction (Schlafly & Finkbeiner 2011) and

converted to luminosities in the host frame. We directly calculate Balmer-decrement extinction, [N II]/Hα, R_{23} (Pagel et al. 1979), and the gas-phase oxygen abundance values ("metallicities") associated with the latter two using the empirical derivation of Nagao et al. (2006). Electron-temperature (T_e) metallicities are also calculated for the subset of hosts in which the auroral [O III] λ4363 line is detected using the iterative method of Izotov et al. (2006). Uncertainties in all of these values are calculated by performing 1000 Monte Carlo trials using the measured flux uncertainties. In addition, we use the code of Bianco et al. (2016) to calculate metallicities and Monte Carlo uncertainties using a range of additional diagnostics and calibrations (specifically, those of Denicoló
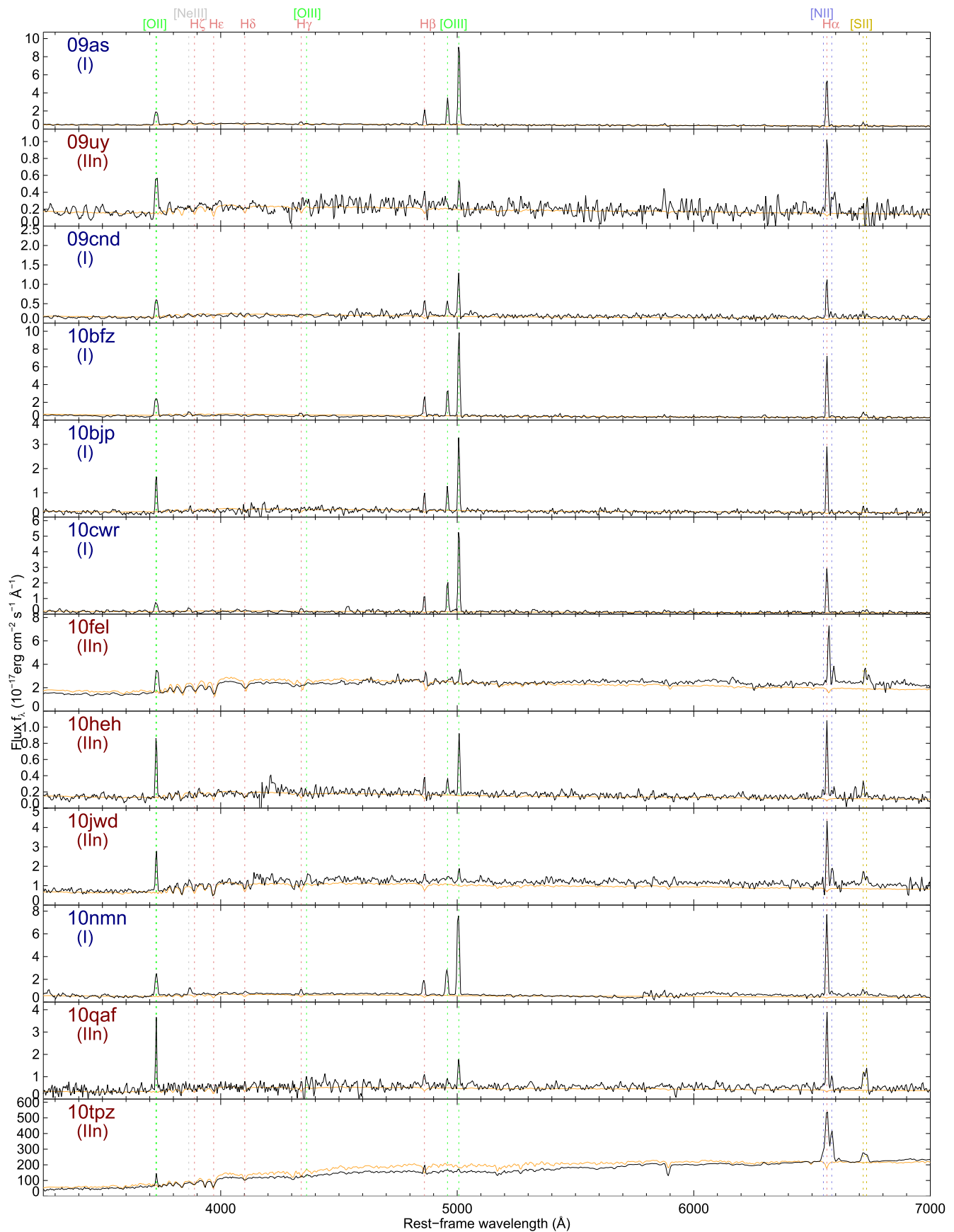
Figure 3. Keck spectra of the host galaxies of PTF SLSNe with clear continuum and/or line detections. (The spectrum of PTF 10tpz shows the nuclear region only.) Overplotted in light orange is the best-fit SED model for the underlying stellar continuum (Section 3.5); this may differ somewhat from the observed spectrum for large galaxies where slit-loss effects are significant.
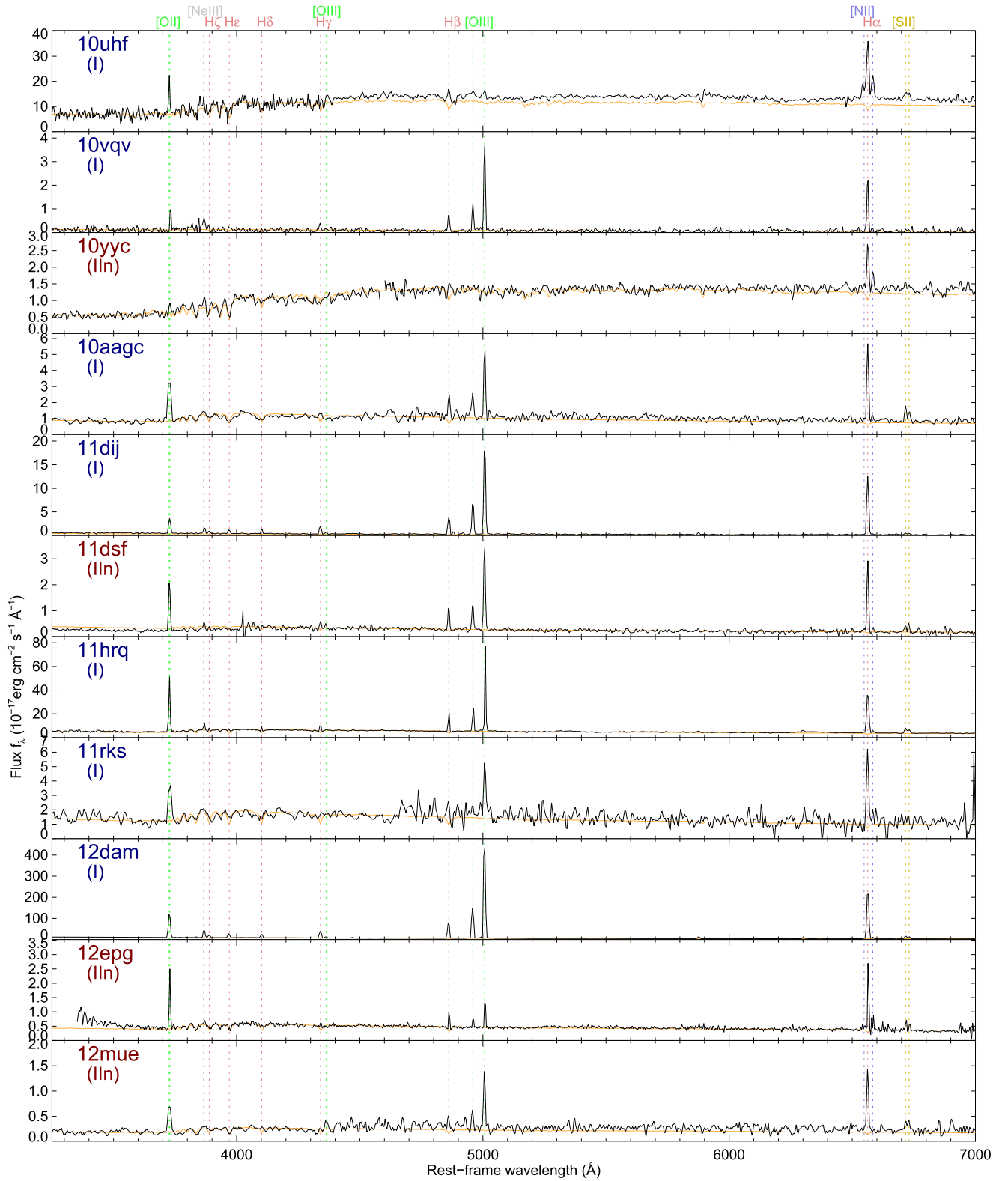
Figure 4. Additional Keck spectra of the hosts of PTF SLSNe with clear continuum and/or line detections. The hosts of PTF 10uhf and PTF 11rks are large and resolved; for PTF 10uhf we show the sum of spectra along two different slit angles (one through each nucleus), whereas for PTF 11rks we display the spectrum obtained from a slit passing through the southern part of the galaxy (not directly intersecting the galaxy nucleus).

et al. 2002; Kobulnicky & Kewley 2004; Pettini & Pagel 2004; Maiolino et al. 2008; Marino et al. 2013; and Kewley & Dopita 2002). SFRs are calculated with the standard conversion of Kennicutt et al. (1987), adjusted for a Chabrier IMF.

3.7. Comparison Samples

In order to help discern to what extent the observed host properties of the SLSN sample reflect the physical influences affecting SLSN production (rather than simply where stars are
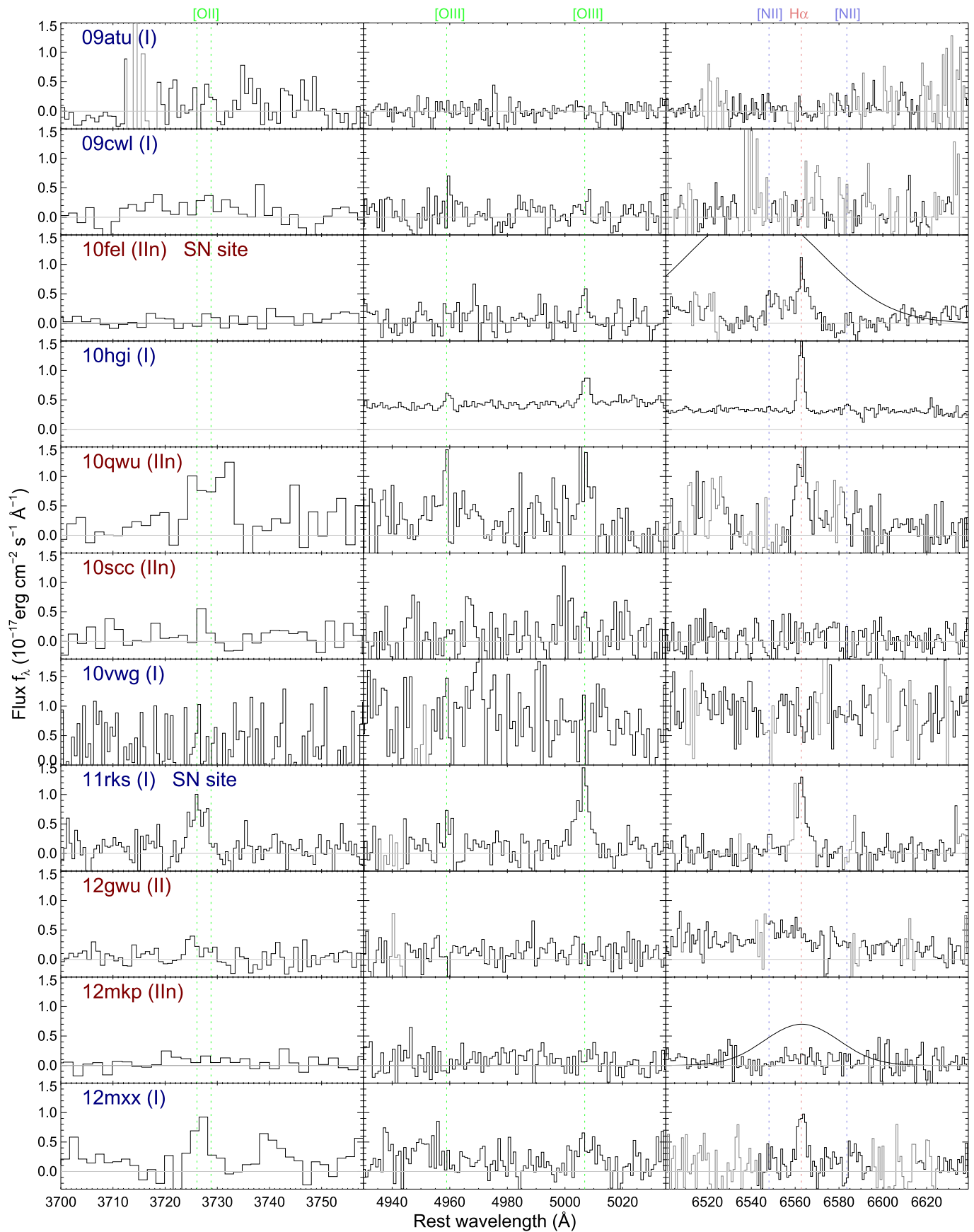
Figure 5. Spectra of SLSN hosts (or SLSN sites) showing no or very faint line emission at the expected locations of the strongest three emission features in typical host-galaxy spectra: the [O II] $\lambda 3727$ doublet (left panel), the [O III] $\lambda\lambda 4959, 5007$ doublet (middle panel), and Hα (right panel; locations of [N II] are also shown). The Gaussian profiles indicate where late-time broad Hα was subtracted from two SLSNe II.

Table 4
Photometric Properties of PTF SLSN Hosts[a]

PTF ID	M_g (AB mag)	SFR ($M_\odot$ yr^{-1})	$\log_{10}(M_*)$ ($M_\odot$)	A_V (mag)	Morphology[b]
09as	−17.72	$1.659^{+0.513}_{-1.490}$	$8.27^{+0.92}_{-0.15}$	$1.34^{+0.08}_{-0.95}$	Compact dwarf
09uy	−17.99	$0.162^{+0.054}_{-0.050}$	$9.24^{+0.11}_{-0.20}$	0	Compact dwarf
09atu	−16.30	$0.528^{+0.332}_{-0.245}$	$8.35^{+0.33}_{-0.62}$	$1.53^{+0.19}_{-0.36}$	Faint dwarf
09cnd	−17.42	$0.481^{+0.203}_{-0.222}$	$8.32^{+0.15}_{-0.18}$	$0.81^{+0.13}_{-0.22}$	Compact dwarf
09cwl	−15.30	$0.015^{+0.005}_{-0.004}$	$7.85^{+0.23}_{-0.33}$	0	Ultra-faint dwarf
10bfz	−17.48	$0.269^{+0.153}_{-0.088}$	$8.65^{+0.11}_{-0.32}$	$0.07^{+0.24}_{-0.07}$	Compact dwarf
10bjp	−18.82	$0.401^{+0.135}_{-0.120}$	$9.21^{+0.15}_{-0.17}$	$0.01^{+0.05}_{-0.01}$	Merger
10cwr	−17.12	$0.532^{+0.287}_{-0.248}$	$7.87^{+0.13}_{-0.21}$	$0.81^{+0.15}_{-0.17}$	Compact dwarf
10fel	−19.88	$0.576^{+0.236}_{-0.210}$	$10.15^{+0.11}_{-0.15}$	0	Disk galaxy (SN in far outskirts)
10heh	−17.99	$0.410^{+0.229}_{-0.143}$	$9.18^{+0.12}_{-0.19}$	$0.42^{+0.19}_{-0.11}$	Compact dwarf
10hgi	−15.92	$0.204^{+0.089}_{-0.076}$	$7.90^{+0.14}_{-0.20}$	$1.24^{+0.11}_{-0.12}$	Faint compact dwarf/disk
10jwd	−19.98	$0.707^{+0.432}_{-0.350}$	$10.25^{+0.11}_{-0.16}$	$0.17^{+0.13}_{-0.15}$	Disk
10nmn	−17.24	$0.229^{+0.074}_{-0.074}$	$8.79^{+0.11}_{-0.15}$	0	Irregular
10qaf	−18.78	$0.268^{+0.123}_{-0.092}$	$9.64^{+0.13}_{-0.16}$	<0.16	Dwarf satellite
10qwu	−16.04	$0.145^{+0.099}_{-0.073}$	$8.09^{+0.21}_{-0.61}$	$0.67^{+0.26}_{-0.29}$	Compact faint dwarf
10scc	−13.57	$0.011^{+0.003}_{-0.003}$	$6.00^{+0.95}_{-0.15}$	0	Ultra-faint dwarf
10tpz	−20.25	$0.082^{+0.581}_{-0.085}$	$10.85^{+0.12}_{-0.15}$	$0.58^{+0.19}_{-0.19}$	Massive early-type
10uhf	−22.09	$6.837^{+2.227}_{-3.103}$	$11.23^{+0.12}_{-0.15}$	$0.29^{+0.10}_{-0.20}$	Large spiral/minor merger
10vqv	−18.53	$2.355^{+0.724}_{-1.229}$	$8.08^{+0.92}_{-0.15}$	$0.73^{+0.05}_{-0.24}$	Compact dwarf
10vwg	−15.07	<0.067	$8.25^{+0.18}_{-0.59}$	0	Compact dwarf
10yyc	−18.92	$0.075^{+0.032}_{-0.037}$	$9.99^{+0.11}_{-0.15}$	0	Disk
10aagc	−18.71	$1.566^{+1.049}_{-0.646}$	$8.98^{+0.13}_{-0.21}$	$0.91^{+0.23}_{-0.18}$	Merger
11dij	−16.55	$0.577^{+0.176}_{-0.182}$	$6.90^{+0.17}_{-0.15}$	$0.65^{+0.07}_{-0.03}$	Compact dwarf satellite
11dsf	−19.09	$3.477^{+1.429}_{-1.454}$	$9.14^{+0.16}_{-0.65}$	$0.69^{+0.17}_{-0.19}$	Compact dwarf
11hrq	−17.31	$0.209^{+0.065}_{-0.108}$	$8.55^{+0.28}_{-0.21}$	$0.46^{+0.07}_{-0.36}$	Disk
11rks	−18.93	$1.064^{+0.346}_{-0.429}$	$9.11^{+0.13}_{-0.16}$	$0.45^{+0.09}_{-0.18}$	Complex, diffuse galaxy/minor merger?
12dam	−19.69	$11.13^{+3.376}_{-3.339}$	$8.30^{+0.15}_{-0.15}$	$0.90^{+0.04}_{-0.02}$	Compact dwarf with extended tidal features
12epg	−19.21	$4.896^{+2.841}_{-3.505}$	$9.27^{+0.14}_{-0.24}$	$1.26^{+0.23}_{-0.44}$	Compact dwarf
12gwu	−16.47	$0.033^{+0.012}_{-0.012}$	$8.75^{+0.12}_{-0.16}$	0	Faint dwarf
12mkp	−13.54	<0.004	$7.58^{+0.12}_{-0.33}$	0	Ultra-faint dwarf
12mue	−17.99	$0.962^{+0.532}_{-0.385}$	$9.15^{+0.12}_{-0.23}$	$0.91^{+0.17}_{-0.17}$	Compact dwarf
12mxx	−16.90	$0.797^{+0.428}_{-0.393}$	$8.16^{+0.61}_{-0.24}$	$1.31^{+0.15}_{-0.36}$	Faint dwarf

Notes.
[a] Properties derived from SED fitting to the photometry in Table 2. Uncertainties are derived from the distribution of Monte Carlo trials plus (for SFR and M_* estimates) an additional systematic uncertainty of 10%. An A_V value of 0 with no uncertainty indicates that this parameter was fixed.
[b] Informal morphological properties from visual inspection and from estimates of the size, luminosity, and environment of each host galaxy.

(This table is available in machine-readable form.)

forming in the low-redshift universe), it is necessary to compare our host galaxies to a representative sample of star-forming galaxies at similar redshifts. The ideal sample for this purpose would provide all of the same measurements available for our hosts (i.e., integrated UV-through-NIR SEDs and optical spectroscopy, and physical parameters derived from these measurements) and be complete down to a comparable luminosity limit to that of our sample ($M_g \lesssim -14$ mag, with no targeting or other systematic biases) over a sufficiently large volume to avoid systematics associated with cosmic variance. Ideally it would also have a similar median redshift ($z \approx 0.3$) to our host sample.

Unfortunately, no single publicly available galaxy sample currently exists satisfying all these criteria simultaneously: most surveys (especially spectroscopic surveys) are complete only to high-mass galaxies and insensitive to the low-mass dwarf galaxies that dominate the SLSN host population. Certain surveys come close in restricted regimes, or can be

made to be (nearly) volume limited by employing a stringent distance cut or cuts. We rely on three different surveys in our comparisons, outlined below.

3.7.1. LVL Galaxies

The Local Volume Legacy Survey (LVL; Dale et al. 2009; see also Kennicutt et al. 2008; Lee et al. 2011; Cook et al. 2014a, 2014b) is a volume-complete sample of galaxies within 11 Mpc. The catalogs include narrowband-imaging-derived Hα fluxes and thorough UV-through-NIR photometry. This catalog has the advantage of being essentially complete down to extremely faint levels for star-forming galaxies and has very thorough and reliable multiwavelength measurements. However, the survey volume is small—subjecting it to both statistical limitations (the survey includes only 313 galaxies in total, and rare classes of galaxies are poorly sampled) and systematic/cosmic-variance effects associated with only sampling a region around the Local Group (devoid of large voids or

Table 5
Emission-line Fluxes for SLSN Hosts[a]

PTF ID	Hα 6563	Hβ 4861	Hγ 4340	[O II] 3727	[O III] 4363	[O III] 4959	[O III] 5007	[N II] 6548	[N II] 6584	[S II] 6716	[S II] 6731
09as	62.9 ± 0.6	18.6 ± 0.7	7.3 ± 0.6	27.7 ± 0.8	2.1 ± 0.5	32.4 ± 0.8	101.8 ± 1.0	0.7 ± 0.4	2.0 ± 0.4	4.3 ± 0.4	2.8 ± 0.4
09uy	11.3 ± 1.6	2.3 ± 0.6	<7.5	8.7 ± 0.7	<6.3	<1.8	4.2 ± 0.6	<2.0	<5.8	<6.3	<3.1
09atu	<1.7	<1.9	<1.3	<3.0	<1.7	<1.1	<1.4	<1.7	<2.1	<5.6	<4.1
09cnd	11.7 ± 0.3	4.7 ± 0.4	1.4 ± 0.4	10.0 ± 0.6	<1.2	4.2 ± 0.5	12.4 ± 1.3	<0.7	<1.9	1.8 ± 0.5	1.4 ± 0.4
09cwl	<1.5	<1.4	<2.0	<1.2	<4.9	<1.3	<1.2	<2.1	<3.8	<1.0	<0.9
10bfz	80.0 ± 0.8	26.0 ± 1.5	9.6 ± 0.7	39.7 ± 1.3	2.6 ± 0.7	34.9 ± 1.3	108.7 ± 1.6	<2.2	2.1 ± 0.5	7.1 ± 1.3	4.2 ± 1.0
10bjp	33.2 ± 0.7	10.6 ± 0.8	<6.9	24.1 ± 0.9	<3.7	13.3 ± 0.8	40.8 ± 1.0	<1.2	<2.9	4.0 ± 0.4	2.4 ± 0.4
10cwr	33.9 ± 0.7	13.1 ± 1.2	5.8 ± 1.1	12.2 ± 1.0	2.9 ± 1.1	22.8 ± 1.1	64.0 ± 1.4	<2.0	<1.6	1.7 ± 0.5	3.0 ± 0.8
10fel[b]	66.0 ± 1.0	18.4 ± 1.1	8.7 ± 0.8	41.0 ± 0.8	<2.4	3.2 ± 0.9	15.4 ± 1.0	4.1 ± 0.9	16.4 ± 0.9	17.5 ± 2.4	9.1 ± 1.0
10fel (site)	5.1 ± 0.6	1.6 ± 0.7	<1.2	<1.2	<1.3	<1.7	2.3 ± 0.6	2.0 ± 0.8	<1.8	<4.2	<1.9
10heh	11.4 ± 0.6	3.2 ± 0.3	1.4 ± 0.3	9.7 ± 0.4	<0.9	2.4 ± 0.3	7.9 ± 0.7	1.2 ± 0.5	0.9 ± 0.2	2.3 ± 0.4	0.8 ± 0.3
10hgi	5.1 ± 0.3	1.4 ± 0.2	0.8 ± 0.3	...	<0.8	0.7 ± 0.2	2.1 ± 0.2	<0.5	0.5 ± 0.2	0.7 ± 0.2	0.5 ± 0.2
10jwd	44.5 ± 1.7	6.8 ± 1.2	5.2 ± 1.4	25.4 ± 0.9	<4.8	2.5 ± 0.9	7.9 ± 0.9	<8.3	12.9 ± 1.4	10.6 ± 1.1	6.1 ± 0.8
10nmn	110.1 ± 1.3	27.6 ± 1.4	12.8 ± 0.9	45.9 ± 1.9	<3.3	47.4 ± 4.2	144.9 ± 1.9	<3.8	5.6 ± 1.2	7.7 ± 0.8	5.1 ± 0.8
10qaf	39.7 ± 1.5	9.7 ± 2.2	<7.3	34.2 ± 1.6	8.7 ± 3.3	4.5 ± 1.9	18.1 ± 1.8	<3.8	3.8 ± 1.6	10.5 ± 2.4	12.6 ± 1.8
10qwu	8.5 ± 1.1	<6.8	<4.7	7.4 ± 1.8	<5.1	3.1 ± 1.5	6.2 ± 1.6	<8.4	<3.1	<2.6	2.3 ± 1.0
10scc	<2.8	<5.3	<3.9	<4.2	<4.0	<4.8	<5.1	<2.7	<2.5	<8.9	<4.2
10tpz (site)	6029 ± 115	1096 ± 23	524.9 ± 16.6	809.0 ± 19.9	<51.3	97.5 ± 21.4	282.9 ± 22.4	972.4 ± 91.2	3173 ± 105	1010 ± 18	742.2 ± 17.8
10uhf[c]	408.6 ± 12.8	87.5 ± 7.8	48.4 ± 15.7	126.0 ± 5.4	<50.1	28.5 ± 6.5	42.7 ± 6.4	66.1 ± 11.5	142.1 ± 8.2	48.0 ± 9.0	35.4 ± 8.5
10uhf (site)	14.2 ± 0.3	2.7 ± 0.3	<2.8	7.1 ± 0.4	1.3 ± 0.6	1.2 ± 0.3	2.5 ± 0.3	2.0 ± 0.2	5.3 ± 0.2	2.9 ± 0.4	2.0 ± 0.3
10vqv	29.7 ± 0.8	9.7 ± 0.7	4.2 ± 2.0	12.8 ± 1.0	<2.7	15.6 ± 0.7	51.1 ± 1.0	<2.7	3.0 ± 0.7	1.5 ± 0.5	0.9 ± 0.4
10vwg	<11.1	<23.2	<20.9	<7.2	<21.4	<23.5	<22.3	<14.2	<8.2	<18.1	<8.2
10yyc	21.7 ± 1.1	6.5 ± 1.5	<4.2	5.2 ± 1.2	<4.0	<4.1	<4.1	3.1 ± 0.9	7.8 ± 1.2	3.8 ± 0.8	2.0 ± 0.7
10aagc	56.7 ± 1.9	17.7 ± 2.0	11.0 ± 1.6	49.1 ± 2.9	<4.5	16.5 ± 2.0	50.6 ± 2.1	2.3 ± 1.0	3.3 ± 1.0	12.0 ± 1.1	7.3 ± 1.0
11dij	141.2 ± 1.6	41.9 ± 1.2	20.0 ± 0.7	40.1 ± 1.5	4.4 ± 0.5	76.5 ± 1.9	209.2 ± 3.4	<2.9	<4.5	3.8 ± 0.4	3.2 ± 0.4
11dsf	31.2 ± 0.6	11.0 ± 0.5	3.9 ± 0.6	22.4 ± 0.5	1.4 ± 0.5	11.8 ± 0.7	38.4 ± 0.6	1.1 ± 0.4	1.9 ± 0.3	2.8 ± 0.4	5.3 ± 1.3
11hrq	420.0 ± 4.4	137.9 ± 3.1	64.0 ± 2.1	342.1 ± 4.8	5.3 ± 1.9	162.2 ± 3.9	462.3 ± 11.6	8.2 ± 2.9	21.9 ± 2.4	47.3 ± 1.6	31.7 ± 1.5
11rks[d]	53.9 ± 3.9	16.8 ± 4.0	11.2 ± 3.8	52.0 ± 4.9	<12.4	<17.3	42.7 ± 4.4	<15.6	<25.4	<6.7	<18.8
11rks (site)	8.7 ± 0.7	2.9 ± 0.8	1.2 ± 0.5	4.5 ± 0.6	<1.6	2.5 ± 0.9	8.2 ± 0.9	<2.4	<2.5	<1.7	<2.4
12dam	2797 ± 16	929.6 ± 40.0	486.4 ± 9.7	1748 ± 23	93.7 ± 7.5	1823 ± 55	5569 ± 97	31.9 ± 6.7	84.7 ± 5.9	177.3 ± 4.2	129.1 ± 2.9
12epg	19.5 ± 0.9	5.8 ± 0.3	2.6 ± 0.3	17.3 ± 0.6	<0.7	2.8 ± 0.2	9.2 ± 0.3	1.7 ± 0.5	3.7 ± 0.5	3.3 ± 0.3	2.4 ± 0.3
12gwu	<0.7	<0.8	<3.7	...	<3.0	<0.7	<0.7	<1.8	<0.7	<0.4	<0.4
12mkp	<1.7	<3.1	<1.5	<1.9	<1.6	<2.1	<2.2	<1.2	<1.2	<1.2	<1.8
12mue	25.9 ± 0.9	6.2 ± 1.3	3.9 ± 1.3	17.1 ± 1.3	9.9 ± 4.6	7.4 ± 1.2	24.6 ± 1.3	<2.1	<3.7	4.0 ± 0.8	3.9 ± 0.7
12mxx	6.4 ± 0.6	3.0 ± 1.0	<4.6	4.5 ± 1.1	<6.0	<2.8	2.7 ± 0.9	<2.6	<1.9	<6.2	2.0 ± 0.7

Notes.

[a] In units of 10^{-17} erg cm^{-2} s^{-1}, corrected for Galactic extinction. 1σ statistical uncertainties shown. These do not include uncertainties associated with the overall flux calibration, which for sources with SN contamination or weak continuum (09atu, 09cwl, 10hgi, 10qwu, 10scc, 10vwg, 12mue, 12mxx) may be significant but will affect all lines proportionally.

[b] For the large disk galaxy near the SLSN position.

[c] From the sum of extractions from a slit through the nucleus of the "major" and "minor" components of the merger.

[d] From a slit that passes through the "primary" galaxy, although not through its nucleus.

(This table is available in machine-readable form.)

clusters). It also samples only the $z \approx 0$ universe and is purely a photometric survey with no spectroscopy, although metallicity measurements are available for about two-thirds of these galaxies from the literature (we employ the compilations in Marble et al. [2010] and Cook et al. [2014b] and add measurements for NGC 1569 and II Zw 40 from Kobulnicky & Skillman [1997] and Walsh & Roy [1993], respectively). Even with these limitations, it is by far the most reliable catalog for examining the contribution of faint, low-mass galaxies to the local SFR density.

3.7.2. Ultra-VISTA Galaxies

The Ultra-VISTA catalog (Muzzin et al. 2013) is a very deep multiband photometric survey in the COSMOS field targeted mainly at high-redshift galaxies. The photometric redshifts obtained by the survey allow it to reach low-mass galaxies at redshifts comparable to those of our SLSN hosts, although it does not provide Hα measurements and it remains incomplete at very low masses: specifically, below $3 \times 10^8 \, M_\odot$ at $z \approx 0.2$. The SED fitting procedure used also appears unable to recognize starburst galaxies since essentially no galaxies with an SFR greater than $>2 \, M_\odot \, \mathrm{yr}^{-1}$ are present within the catalogs at low redshifts (with the exception of a small number of objects that appear to be due to problematic fits since the SED SFRs exceed the direct UV SFRs by an unreasonable factor; these are cleaned from the catalog in our plots/analysis). Nevertheless, the catalog is large (17,932 galaxies at $z < 0.6$), and the stellar mass measurements should be robust, so it provides an excellent complement to LVL to check for the effects of cosmic variance or redshift evolution in the photometric data.

3.7.3. SDSS Galaxies

The SDSS spectroscopic galaxy sample has been extensively used for comparisons to SN and GRB host populations for over a decade, thanks to its extremely wide coverage and high-quality spectroscopy including flux measurements of all the key strong emission lines used for metallicity and other gas-phase analysis (see, e.g., Modjaz et al. 2008; Graham & Fruchter 2013). Despite these advantages, SDSS has several important limitations. First of all, it is relatively shallow: spectroscopic coverage is complete only to $r < 17.77$ mag (Strauss et al. 2002), so it is insensitive to low-mass galaxies except at very low redshifts.[17] Because of the survey's vast areal coverage, it can simply be restricted to quite low redshifts (where it is complete to lower-mass galaxies) and still maintain a large sample size. However, at low redshifts two other challenges come into effect. First, the wavelength range of the survey does not cover the [O II] line (needed for R_{23}-based metallicity derivations or ionization-parameter analysis) at redshifts below $z < 0.021$. Even more importantly, SDSS spectroscopy is based on fibers of limited area: 3″ diameter or 1″.5 in radius, meaning that at low redshifts essentially only the galaxy nucleus is covered ($r < 300$ pc at $z = 0.01$). As a result, a significant tension emerges—the high-z subset is incomplete to the low galaxy masses relevant to our SLSN hosts, but the low-z subset is highly fiber-biased, causing it to (in particular) overestimate metal abundances and underestimate SFRs due to

systematic differences between the nucleus and the disk in typical large galaxies.

We attempted to mitigate these issues by adopting a hybrid approach to selection, using different redshift ranges to sample different mass ranges. As our base catalog, we utilize the NASA-Sloan Atlas (NS-Atlas[18]) reanalysis of the SDSS spectroscopic sample, a re-reduction of the main galaxy sample (at $z < 0.05$) with improved sky subtraction and spectroscopic analysis, as well as mass measurements based on SED fitting to the $GALEX+ugriz$ photometry. We then take five different mass–redshift slices (each of the same cosmic volume): $z = 0.0025–0.0085$ for $M_* < 10^7$, $z = 0.005–0.009$ for $10^7 < M_* < 2 \times 10^8$, $z = 0.01–0.0117$ for $2 \times 10^8 < M_* < 1 \times 10^9$, $z = 0.025–0.02532$ for $10^9 < M_* < 5 \times 10^9$, and $z = 0.0450–0.0451$ for $M_* > 10^9$, leaving a final sample of 1497 galaxies complete down to $\sim 10^7 \, M_\odot$. Even with these corrections, the fiber covers only the central region of each host ($r < 50, 100, 200, 500,$ and 880 pc, respectively, for each redshift bin), and metallicity- and specific SFR-gradient effects are likely to be large. We therefore generally favor the smaller LVL sample in our analysis, except in cases where knowing the individual measured line fluxes is necessary (Section 5.5).

4. DISCUSSION OF INDIVIDUAL OBJECTS

4.1. PTF 09as

This event was found very early in the survey but was initially misclassified as an SN Ia and not recognized as an SLSN until 2015 (6 yr after discovery) after reanalysis of archival PTF spectra (R. Quimby et al. 2016, in preparation). Accordingly we have no late-time imaging, but the host is detected in SDSS pre-imaging (in g, r, i, and marginally in z); the host appears only marginally resolved. Our LRIS spectrum of this galaxy shows a modest continuum and strong emission from all major nebular lines.

4.2. PTF 09uy

A moderately faint, unresolved source is visible underlying the SN position in late-time MOSFIRE and LRIS imaging, which we identify as the host galaxy. Spectroscopy shows emission lines of [O II], [O III], Hα, [N II], and [S II], as well as strong continuum from a more mature stellar population. There is no evidence of an AGN contributing to the flux, supporting our identification of the transient as an SLSN.

4.3. PTF 09atu

Discovery imaging and classification spectra of this event were previously presented in Quimby et al. (2011), along with those of PTF 09cnd, PTF 09cwl, and PTF 10cwr. It is the most distant event in our sample, with a redshift of $z = 0.501$ (well determined by narrow Mg II absorption in the original SN spectra; Quimby et al. 2011). Late-time imaging with Keck and *HST* detects a persistent source within 1″ of the SN location, but it is very faint ($R \approx 26$ mag) and the detections in each filter are individually marginal. Cumulatively, the detections are significant, and we identify this target as the probable host galaxy, although given its offset and faintness we cannot completely rule out that it is a chance coincidence (in which

---

[17] This completeness is also limited to objects morphologically classified as galaxies, meaning that it may accidentally exclude compact, high-surface-brightness galaxies as stars.

[18] http://www.nsatlas.org/

case the host would be even fainter.) Keck spectroscopy over the putative host location shows neither any detectable continuum nor any lines at the expected wavelengths of strong galaxy emission features given the SN redshift (or elsewhere in the spectrum), indicating a low-mass galaxy not in a starburst phase.

4.4. PTF 09cnd

The SN is located on the northeast fringe of a compact, moderately bright galaxy visible in our late-time multicolor imaging. Spectroscopy reveals a strong continuum with various strong emission features superimposed at a redshift consistent with that of the narrow Mg II absorption in the early-time spectrum. A neighboring source ($2\farcs2$ from the host) is also seen in our imaging; the slit was aligned to cover both sources, but the companion shows no strong emission or absorption lines, so its redshift or association with the host is unknown.

4.5. PTF 09cwl (SN 2009jh)

The host galaxy of this event is extremely faint ($R \approx 26$ mag). No significant flux at the wavelengths of any expected strong emission line features is evident in our spectroscopy.

4.6. PTF 10bfz

The host of this event is well detected in our imaging, it is unresolved, and there are no nearby companions. Strong nebular emission lines are evident, indicating a compact, low-mass galaxy undergoing active star formation.

4.7. PTF 10bjp

The appearance of two distinct sources connected by a bridge of emission strongly suggests that this host galaxy is undergoing a major merger; spectroscopy confirms that they are at the same redshift. Both are strongly star-forming. We report the combined fluxes of both galaxies (and treat the two galaxies as a single object) throughout the paper. The SN occurred in the southern member of the pair.

4.8. PTF 10cwr (SN 2010gx)

The host galaxy is bright and compact in our imaging and directly underlies the SN position, although a second object is easily visible in the imaging $\sim 1''$ east of this location. While our late-time host galaxy spectrum was not oriented to cover this object, an earlier spectrum of the SN did place this object on the slit and shows it to be a star-forming galaxy in the background at $z = 0.622$ and therefore unassociated. The host itself is strongly star-forming and shows a clear detection of the [O III] $\lambda 4363$ auroral line, marking it as quite metal-poor: indeed, it is the most metal-poor galaxy among all members of our sample for which spectroscopic measurements are available. (These properties were also remarked on by the dedicated study of Chen et al. 2013.)

4.9. PTF 10fel

Imaging of the field shows a complex region surrounding the transient location. A massive disk galaxy is evident $\sim 4''$ southeast in projection from the SN location (with the offset nearly aligned with the galaxy's major axis); two faint pointlike sources are visible $\sim 1''$ north and $\sim 4''$ northwest of the SN

location (respectively), and some faint, diffuse emission surrounds the entire region. The SN itself is not coincident with any of the individual objects.

A late-time spectrum aligned with the SN location and the closer of the two point sources shows no detectable emission at the SN site but weak emission from the point source at a much higher redshift, indicating that this source is unassociated. An earlier, deeper spectrum of the SN itself shows faint narrow Hα emission at the SN location after the broad Hα line from the SN is subtracted.

We treat the nearby disk galaxy as the "host" for our purposes—although it is possible that the SN is actually associated with an extremely faint unseen satellite. Even if the SN is associated with this galaxy, it evidently occurred in a location that is not representative of the star-forming conditions probed by our spectroscopy of that galaxy, and so the properties we report for this system should be used with caution when drawing conclusions about the host population.

4.10. PTF 10heh

The host is not significantly resolved by our imaging observations. It shows a weak continuum and strong emission features, indicating an actively star-forming low-mass galaxy.

4.11. PTF 10hgi

This is one of the most nearby events in the sample at $z = 0.098$. The host is well detected in ground-based imaging and resolved into a disk-like structure, although it has a very low luminosity ($M_g \approx -16$ mag). The emission lines from this galaxy are quite weak, clearly demonstrating that SLSNe can form in dwarf galaxies outside of their starburst phases. It may be a good analog of more distant (and harder-to-study) low-luminosity hosts such as PTF 09atu and PTF 09cwl.

4.12. PTF 10jwd

The host of this event is quite bright; morphologically this event resembles a resolved, nearly edge-on disk similar to PTF 10hgi with a hint of some asymmetry. The spectrum is dominated by an older population with a clear Balmer break, although significant emission lines are present also—including moderately strong [N II] and [S II].

4.13. PTF 10nmn

Because the redshift of this event places several of the critical strong nebular emission lines near the half-power point of the LRIS D560 dichroic, this host galaxy was instead observed using the lower-resolution B300 grating and the D680 dichroic. Unfortunately, this introduces some additional complications associated with second-order light (both the host and the standard star observed in this setup are relatively blue), complicating the flux calibration. This mainly affects the region of the spectrum between approximately 6000 and 6600 Å (5300–5900 in the host frame), where there are no strong lines of interest, although it does impede accurate calculation of the relative scaling between lines redder than this (Hα, [N II], and [S II]) and the remaining lines.

The host is small and only marginally resolved by ground-based imaging, which shows a central core with extensions in various directions. The HST imaging resolves the core into a diffuse structure and situates the SN about $1''$ southwest of the

galaxy center, along a narrow extended structure (possibly a tidal feature). The LRIS slit was aligned with the host center and the SN site; while strong nebular emission is present throughout the host along this slit, all emission lines are much stronger in and around the location of the SN site while the underlying continuum is much weaker, indicating that the SN occurred in a particularly young and active star-forming region.

To be consistent with the rest of our analysis, and because the star-forming region at the SN site dominates the nebular emission of the host overall, we extract the spectrum of the entire host galaxy. The marginally resolved nature of the host permits some spatially resolved analysis that will be reported by O. Yaron et al. in forthcoming work.

4.14. PTF 10qaf

PTF 10qaf occurred in a dwarf companion to a large, face-on spiral galaxy with which it is presumably interacting (our spectroscopy confirms it to be at the same redshift), although the two galaxies are physically separate and do not appear to be actively merging. The host has previously been studied by Leloudas et al. (2015), although they do not distinguish that the host and its neighbor are separate galaxies (they do extract the host separately in their spectroscopy and refer to it as the SN site). The host has strong emission lines but is not remarkable, and the strong detections of [N II] and [S II] (and relatively weak [O III] $\lambda\lambda4959, 5007$) suggest that it is neither starbursting nor particularly metal-poor.

4.15. PTF 10qwu

The field surrounding the location of 10qwu is complex. Three unresolved/marginally resolved sources appear close to the SN site: the faintest of these is coincident with the SN, a slightly brighter source is separated by $1''$ to the southeast, and a second, even brighter source is separated by about $2''$ to the southwest. The slit was oriented to cover the fainter two sources. We detect no continuum or line emission at the faintest of these (the SN site). At the neighboring, brighter source we detect marginal continuum emission and weak lines corresponding to Hα, [O II], and [O III], at a redshift equivalent to that determined from the narrow-line emission from the SN at earlier times. We treat this object as the host galaxy (with the SN site on a faint extension), although it is possible that the two are not connected and only the underlying source is the host galaxy, in which case it would be much fainter than as presented here.

4.16. PTF 10scc

The host galaxy of this event is (along with PTF 12mkp) the least luminous in the sample: despite a relatively nearby redshift of $z = 0.242$, the host is only weakly detected in deep Keck imaging; the inferred absolute magnitude is $M_g = -13.5$. As with other very faint hosts, spectroscopy at this location shows no significant emission lines at this position.

4.17. PTF 10tpz

This SN is unusual in many regards (see also Section 2.4). It is the nearest event in the sample by a large margin, it is highly extinguished (without an extinction correction it would seem far from superluminous), and it is located very close to the nucleus of a massive early-type galaxy (adaptive optics

imaging, to be presented in future work, demonstrates that it does not originate from the nucleus itself). These properties call to mind SN 2006gy (e.g., Smith et al. 2007) and candidate SN CSS 100217 (Drake et al. 2011) and are completely distinct from any other host in our sample, possibly suggesting that this event belongs to a distinct progenitor class from the others presented here.

Both the continuum and nebular flux of the galaxy are dominated by the inner region where the SN occurred, and for this particular host galaxy we extract only this innermost region.[19] The [N II]/Hα ratio in this spectrum suggests that an AGN is present, making this the only host galaxy in our sample containing an (observable) AGN. The very weak [O III] emission suggests that the AGN is subdominant, however, and the observed nuclear flux likely originates from a mixture of star formation and AGN activity (Bamford et al. 2008). We ignore this unknown AGN contribution in our line analysis, but we emphasize that [N II]-based estimates of the metallicity are unreliable and the true Hα SFR will be somewhat less than our analysis implies.

4.18. PTF 10uhf

At a glance this host appears unique in our sample (see Figure 1) as the only large grand-design spiral. The SN site is located $4''$ (17.5 kpc) from the host's center in an extended arcing feature resembling a spiral arm. However, careful examination of the images reveals a second nucleus $2''$ northwest of the primary nucleus and a second pair of "arms" with a similar sigmoid shape to those of the primary spiral. Most likely this system represents the merger of a massive spiral galaxy with a somewhat less massive disk galaxy, with both objects pulled into a distorted shape by the interaction. The SN itself cannot be unambiguously associated with either system; its location is at the overlap of the northern "arms" of both galaxies.

We obtained spectroscopy with the slit oriented between the SN site and the nucleus of the "major" galaxy, as well as with the slit aligned to cover the "minor" merging companion in the interaction. Nebular emission is detected throughout the positions of the galaxy on both slits, including at the SN site. Due to the difficulty of concretely associating the SN with either component individualy and the fact that the galaxy pair would be treated as single by most surveys, we treat the two galaxies as a single object and report their properties together (using a large aperture, and summing our slits along both axes). We also extracted a spectrum at the SN location exclusively, excluding the galaxy nuclei.

While the star formation intensity is moderate throughout (e.g., the [O III] line is weak throughout both slits, including at the SN site), the cumulative flux of Hα and [O II] is very high and the Hα/Hβ ratio indicates a significant extinction correction, making this host both the most massive and the most rapidly star-forming in the sample by a large margin (it is probably a luminous infrared galaxy [LIRG]). Indeed, it appears as an outlier in almost every parameter when compared to other SLSN I hosts—which may suggest that it may be more reasonable to attempt to associate the SN with the "minor"

---

[19] Because of the very extended nature of this galaxy, most of the light from the disk is not contained within the slit, and extracting the entire galaxy would make only a modest difference to the resulting spectrum but would greatly degrade the S/N. Accurate characterization of the entire host will require integral field spectroscopy or other special techniques.

component exclusively. However, even if we made this association, it would reduce the mass and SFR only by approximately a factor of 3–4 (and not significantly alter the metallicity or other line parameters) and it would remain an outlier.

4.19. PTF 10vqv

The host of PTF 10vqv is isolated and generally unresolved, although a faint extension is visible to the south. The SN site is coincident with the host's brightest region. The spectrum shows weak continuum and very strong star formation dominated by intense [O III] emission.

4.20. PTF 10vwg (SN 2010hy)

This event was discovered by KAIT/LOSS (and observed by PTF) in a moderately crowded low-Galactic-latitude field with significant foreground extinction ($A_V = 1.45$ mag). Our initial ground-based optical imaging (in relatively poor seeing conditions of $1\rlap{.}''1$) suggested that the event originated in the apparent outer regions of a diffuse structure, which appeared at the time to be a candidate host galaxy. Subsequent imaging with MOSFIRE under superior seeing conditions and image quality resolved this source into three separate point sources—most likely, foreground Galactic stars—all of which are separated from the host (the offset of the nearest source is approximately $0\rlap{.}''8$). Faint emission can be seen under the SN location only in J band, which presumably represents a very faint "true" host galaxy. A spectrum with the slit oriented across the optically blended stars and the SN location shows no detectable emission features at any point. Most likely this event represents an underluminous, non-intensely star-forming host similar to several of the others discussed above, although the optical blending (and foreground extinction) prevents equivalently deep limits from being provided.

4.21. PTF 10yyc

Imaging of this field shows two bright, resolved disk galaxies with a similar orientation separated by about $2''$. The SN site is coincident with the outer part of the western, fainter (and redder) galaxy. We obtained a spectrum oriented across the nuclei of both galaxies. Despite the small offset, they are not at the same redshift and are unassociated: the host of the SN is at $z = 0.2146$ (consistent with the SN redshift), while the eastern source is in the foreground at $z = 0.198$. The host has a relatively old stellar population and is only modestly star-forming, with strong Balmer absorption lines; weak Hα, [O II], [N II], and [S II]; and only marginal [O III] emission.

4.22. PTF 10aagc

The host of this SN is quite bright and shows clear morphological structure at the resolution of our ground-based imaging—suggesting a possible ongoing merger, although the emission lines are only weakly resolved (<100 km s^{-1}) and the morphology could also be interpreted as a particularly asymmetric dwarf spiral galaxy. Strong emission lines and continuum are both present in the spectra.

4.23. PTF 11dij (SN 2011ke)

This source is (along with PTF 12dam) a classic example of the "extreme emission-line galaxies" discussed among the

SLSN I hosts in Leloudas et al. (2015) (and Lunnan et al. 2014); it has already been discussed in some detail in these works as an intensely star-forming, low-metallicity, compact galaxy. It is part of a small group, with a disk galaxy offset by a few arcseconds,[20] although there are no obvious signatures of interaction in the morphology.

4.24. PTF 11dsf

The host is compact, isolated, and relatively bright. The 2D spectrum shows numerous strong nebular emission lines; their relative fluxes are fully consistent with a star-forming galaxy with no significant AGN contribution. *HST* imaging resolves the host into a small irregular galaxy with no clear point-source nucleus (Angus et al. 2016), and the transient is located off-center, further supporting the SN interpretation of the transient.

4.25. PTF 11hrq

This is the nearest event in the sample (excluding the circumnuclear PTF 10tpz). The host is well resolved in the imaging and is unremarkable, appearing as a partially edge-on disk with no obvious structure. The host exhibits strong emission lines but is not particularly young or starbursting: high-order Balmer absorption features are evident in the continuum, and the line equivalent widths are moderate.

4.26. PTF 11rks

The large galaxy nearest PTF 11rks (at the same redshift, and identified as the host by, e.g., Lunnan et al. 2014 and Angus et al. 2016) is an extended object with hints of complex structure that may suggest a post-merger system or an otherwise turbulent recent history, although it is not particularly actively star-forming anywhere. The SN site is highly offset (by $2\rlap{.}''8$, or 9.2 kpc) from the nucleus, located on top of an extended ($\sim 4\rlap{.}''5$ or 15 kpc long) linear feature in the ground-based imaging. The nature of this feature is unclear: it could be an outer spiral arm or a lower-mass companion galaxy seen edge-on. A zeroth-order image associated with an *HST* grism observation (R. Quimby et al. 2016, in preparation) shows a faint arc connecting this feature to the host nucleus reminiscent of a spiral arm, so it is reasonable to assume that it is "part" of the nearby galaxy. We will follow earlier authors in treating that galaxy as the host, but it is also quite possible that these are tidal tails produced by interaction between two physically distinct galaxies. The large ("host") galaxy is of moderate mass, weakly star-forming, and not metal-poor.

We oriented our slit through the SN site, along the direction of the linear feature. We detect faint stellar continuum, along with weak emission lines of Hα, [O III], and [O II] that are seen only at the SN site and not elsewhere in the companion. The [O III]/[O II] ratio is modest and does not suggest a particularly intense starburst. The redshift is the same as that of the nearby large galaxy. Since the slit does not cover any other part of the "host" in this orientation, we use an earlier spectrum of the SN whose position angle intersected the galaxy just south of its nucleus for our more detailed analysis.

---

[20] This disk galaxy is referred to as a "tadpole tail" and treated as part of the host system by Leloudas et al. (2015), but it appears to be a separate object. Spiral arms are visible in our g-band image, suggesting that it is a highly inclined spiral. The true host is likely a satellite of this object; spectroscopy confirms the two galaxies to be at consistent redshifts.
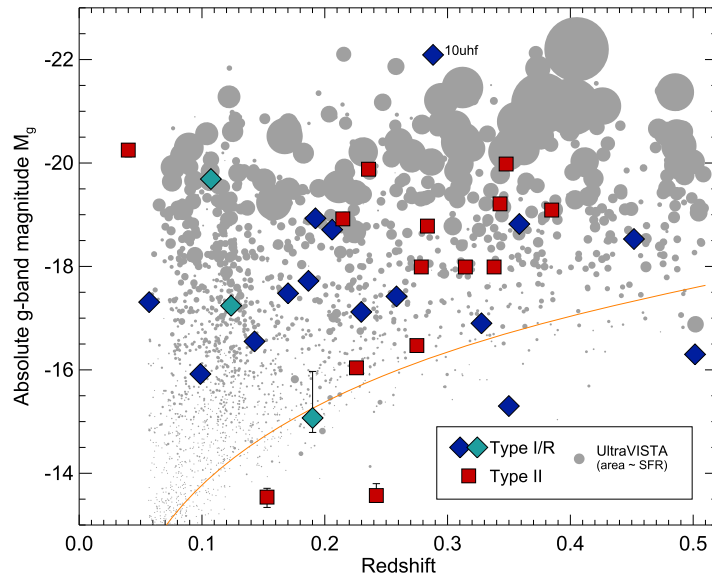
Figure 6. Absolute g-band magnitudes of SLSN host galaxies from PTF as a function of redshift, determined by synthetic photometry of our best-fit model SEDs (Section 3.5). A large sample of star-forming galaxies from Ultra-VISTA is shown in gray, with their sizes scaled according to SFR. The orange curve indicates an apparent magnitude of $m = 24.5$, roughly marking the optical completeness threshold of Ultra-VISTA. The SLSN I host population is dominated by low-luminosity galaxies at all redshifts.

4.27. PTF 12dam

PTF 12dam is among the closest SLSNe to date and took place in a particularly intensely star-forming galaxy with very strong emission lines, and as a result this event has already been the subject of a variety of studies (Lunnan et al. 2014; Chen et al. 2015; Leloudas et al. 2015; Thöne et al. 2015). The stellar population is quite young and the host metal-poor.

To supplement the existing data, we provide *HST* UV imaging and deep ground-based optical imaging. The inner portion of the galaxy resolves into a series of star-forming knots, while the deep optical imaging shows low-surface-brightness extensions in various directions, most prominently a large diffuse component to the southeast but fainter arcs to the north and west— suggestive of tidal features in the advanced phase of a merger.

4.28. PTF 12epg

The host appears compact in our imaging with no close companions. The host is rapidly star-forming, and its spectrum shows bright underlying continuum and nebular lines, although its properties are not extreme.

4.29. PTF 12gwu

The apparent host galaxy is compact and isolated in our imaging. No fully SN-uncontaminated spectrum is available, but a deep observation late in the nebular phase detects weak continuum with a very faint, broad Hα SN feature super-imposed. No narrow emission lines from the host are present at the wavelength of Hα or anywhere else in the spectrum.

4.30. PTF 12mkp

The host is unresolved and faint in our late-time imaging. Two much brighter galaxies are visible in the image at an offset of a few arcsec we aligned our slit with the nearer of the galaxies and find it to be at a different redshift and therefore unassociated. Broad Hα emission from the SN was still present as of 2015 January at the time of our last spectrum (this is

subtracted via a Gaussian fit in Figure 5 for clarity), but no narrow host feature is superimposed, nor are other strong emission features detected.

4.31. PTF 12mue

The host is compact and isolated. Strong emission lines are present on top of a significant continuum from a more evolved population.

4.32. PTF 12mxx

The host of PTF 12mxx is faint and not clearly resolved at the resolution of ground-based imaging. In our spectroscopy we detect weak lines of Hα, [O III], [O II], and marginal continuum.

5. RESULTS

The host properties of the SLSN sample are broad, spanning the full range experienced by local star-forming galaxies. Our primary science objective—understanding whether SLSNe preferentially occur in certain types of galaxy over others (and what these preferences are)—requires quantative compar-ison of the distributions of these physical parameters versus the *expected* distributions as inferred from observations of large, complete samples of star-forming galaxies. This is easier (and more physically informative) for some parameters compared to others, and we will begin this section by qualitatively examining some basic observational properties before proceed-ing to more quantitative comparisons of the key physical parameters that might constrain SLSN progenitor models.

5.1. Detectability, Luminosity, and Color

The term "hostless" is frequently applied to individual SLSNe, indicating that they do not show any evidence of a host galaxy in pre- or post-imaging. Of course, it would be extremely surprising if any SLSN was truly hostless: their large ejecta masses (Nicholl et al. 2015) require an association

with massive stars that cannot feasibly travel significant distances from the environment in which they (and, unavoidably, large numbers of other stars) would have formed. Furthermore, the detection of weak narrow Mg II absorption (at higher redshifts where this is possible with ground-based spectroscopy; Quimby et al. 2011; Vreeswijk et al. 2014) implies at least some preexisting circumgalactic matter.

While many of the host galaxies in our sample are exceptionally low in luminosity, our observations confirm that all SLSNe are indeed hosted within galaxies. Perhaps more usefully, our observations also establish the luminosity scale of several of the faintest SLSN hosts that previously had avoided detection: the faintest hosts in our sample (10scc and 12mkp, both of Type II) have absolute magnitudes of a remarkable $M_g \approx -13.5$ (Figure 6), putting them in the regime of the faintest known actively star-forming galaxies anywhere in the universe.

The association of SLSNe with massive stars also implies that all of their hosts should have active star formation. The lack of detectable emission lines from many of our systems might therefore be seen as surprising. However, these nondetections all correspond to the faintest galaxies in the sample, and the limits on the equivalent widths of these lines by comparing our flux limits to the continuum estimated from the photometry do not rule out that they are star-forming at a steady (nonbursting) rate. Indeed, the broadband colors of all of our ultra-faint hosts are blue, indicating that young ($\lesssim 100$ Myr) stars are present and that steady, low-level star formation is occurring.

Luminous host galaxies are rare in the sample, particularly among the SLSNe I. Only two SLSN I hosts have luminosities exceeding $M_g \approx -19$ mag: the host of PTF 12dam (a very young and intense starburst that is not at all representative of luminous galaxies) and the host of PTF 10uhf (an outlier in our sample and indeed one of the most luminous galaxies in the entire low-redshift universe). Both these systems will be discussed in more detail later.

Quantitative comparisons against the expected parameter distributions for an SN population that traces star formation uniformly will be deferred to further sections. We remark, for now, that simple visual inspection of the vertical positions of SLSNe I in Figure 6 demonstrates that these hosts are not at all typical of the sites of most cosmic star formation (gray points; the area is scaled in proportion to SFR as a visual indicator of their probability of producing an SN per unit time). Cosmic star formation in the local universe is dominated by high-luminosity ($M \approx -20$ mag) galaxies, confirming that the preference for "faint" galaxies (first noted by Neill et al. [2011] and also remarked on by nearly all subsequent work on the topic) is a physical effect evident even in complete single-survey samples.

5.2. Morphology

As our observations were conducted (primarily) by ground-based observatories at a variety of wavelengths and seeing conditions (and many of the hosts are not resolved), it is not straightforward to classify the sample morphologically or easily quantify the host sizes, nor is there an appropriate volume-limited comparison sample to which such measurements could be easily compared. Even so, it is worth briefly and informally remarking on the morphological properties of our sample.

Most SLSN hosts are small galaxies: inspection of Figure 1 demonstrates that most of our sources are marginally resolved
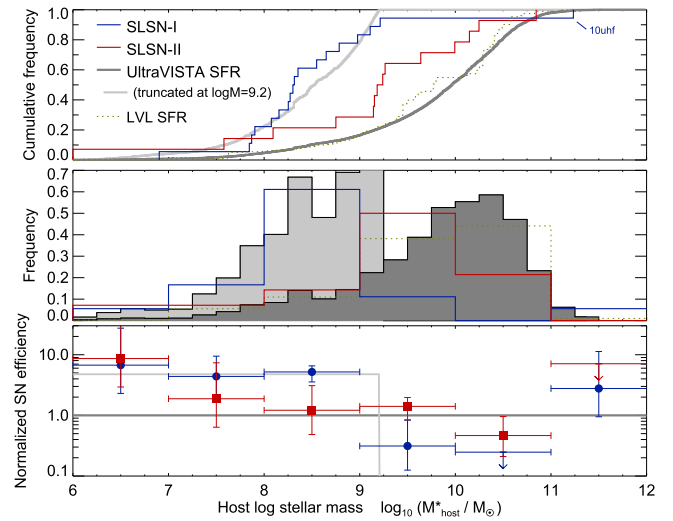

Figure 7. SLSN host-galaxy mass distribution of our sample, compared to the cosmic SFR distribution as a function of M_* measured by galaxy surveys (Ultra-VISTA and LVL). Top panel: cumulative distributions. Middle panel: histograms, expressed as a frequency per 1 dex bin in M_*. Bottom panel: relative SLSN production efficiency per unit SFR, calculated by dividing the SLSN frequency histogram by the SFR frequency histogram and normalizing to an average value of 1.0. In all three plots, the light-gray curve shows a truncated sample from Ultra-VISTA in which galaxies with $\log_{10}(M*/M_\odot) > 9.2$ are neglected. The SLSN I mass distribution shows good consistency with this model, suggesting that these events are strongly suppressed in high-mass galaxies (but their production efficiency is independent of host mass below $\sim 10^{9.2} M_\odot$.) The efficiency of producing SLSNe II does not show strong dependence on stellar mass.

at best, indicating that nearly all of the flux is within a few kiloparsecs of the center (typical seeing conditions of $1''$ correspond to ~ 2 kpc at $z = 0.1$ or ~ 6 kpc at $z = 0.5$). This is consistent with the previous results of Lunnan et al. (2015), who measured a median half-light radius of only 0.9 kpc for SLSN I hosts in the Pan-STARRS sample. Exceptions, where they exist, are fairly dramatic: PTF 10tpz, PTF 10uhf, PTF 10fel, and PTF 11rks are all very large galaxies spanning tens of kiloparsecs in diameter, and in all of these cases except the first the SLSN site is highly offset from the nucleus.

Among the sources that are resolved, mergers are quite common: the hosts of PTF 10bjp, PTF 10cwr, PTF 10uhf, PTF 11rks, PTF 11dij, and PTF 12dam all show binarity, companions, and/or probable tidal features. PTF 10aagc may also be a merger. All of these are SLSNe I; no mergers are evident in the SLSN II sample (note that the apparent companion of PTF 10yyc is actually a foreground galaxy).

5.3. Stellar Masses

Given their characteristically low luminosities, it is not surprising that SLSN I hosts are also strikingly low in mass. The median SLSN I host mass is only $2 \times 10^8 M_\odot$ (less than the mass of the SMC), and every SLSN I host in the sample except that of PTF 10uhf is in a galaxy with $M_* < 10^{9.5} M_\odot$ (approximately the mass of the LMC). SLSNe II are also found in very low mass hosts on occasion, but in contrast to SLSNe I, their hosts appear to populate the entire mass distribution of star-forming galaxies fairly uniformly, including the most massive end (although note our remarks about the local environments of PTF 10tpz and PTF 10fel; Sections 4.17 and 4.9).

The distribution of cosmic star formation with respect to galaxy stellar mass can be evaluated by binning all galaxies from a volume-limited comparison survey in log-mass space, each weighted by their measured SFRs. The Ultra-VISTA catalog provides the best comparison sample for this purpose (due to its large volume and the ability to target the same redshift space at which our SLSNe are actually found), although it does suffer the difficulty that at high redshifts it is incomplete to low-mass galaxies (this effect can be easily seen in Figure 6). In order to sample the full mass and volume range accessed by Ultra-VISTA, we divide the sample into two segments: specifically, we use a redshift range of $z = 0.06$–0.12 to sample the lowest-mass ($<6 \times 10^8 \, M_\odot$) galaxies (Ultra-VISTA is complete to $7 \times 10^7 \, M_\odot$ over this range) and $z = 0.12$–0.5 to sample the higher-mass ($>6 \times 10^8 \, M_\odot$) galaxies, and we reweight the SFRs appropriately to correct for the different volumes sampled.

The resulting distribution is plotted in the middle panel of Figure 7 as the filled histogram. Low-redshift star formation is dominated by galaxies within about 1 dex of $10^{10} \, M_\odot$, with a tail extending to lower masses (in agreement with previous studies, e.g., Brinchmann et al. 2004). As a check on our procedure, we also plot the distribution of the LVL sample and find it to be consistent with the Ultra-VISTA sample (dotted line), demonstrating the effectiveness of our scaling procedure and confirming that the mass threshold of our Ultra-VISTA sample roughly matches the "real" mass threshold below which the contribution to current star formation is no longer significant. Likewise, this demonstrates that redshift evolution over this period is relatively minor.[21]

This distribution can be compared directly to the mass distributions of our host galaxies, which are also plotted as the solid, colored (and unfilled) curves. The peak of the SLSN I host mass distribution at 10^8–$10^9 \, M_\odot$ is clearly much lower than what would be expected for a transient population that traces low-z star formation. This can be expressed statistically by comparing the cumulative distributions, shown in the top panel: a two-sided K-S test gives a probability of 2×10^{-9} that the SLSNe I are drawn uniformly from cosmic star formation. The distribution of SLSN II hosts is much less concentrated toward low-mass galaxies but does exhibit a more modest trend toward low masses that is marginally significant (1.0×10^{-2} of being drawn from random chance). The distributions of the two SLSN populations are also significantly different from each other (3×10^{-3} chance significance).

More interesting than the simple fact that the SLSN I host population is skewed toward low-mass galaxies (which has also been noted by others; e.g., Lunnan et al. 2014; Leloudas et al. 2015) is the nature of this skew: i.e., is it a preference for the lowest-mass galaxies, an aversion against the highest-mass

galaxies, or some combination? The ratio of the SLSN versus SFR histograms is plotted in the bottom panel of Figure 7: this shows the SLSN rates per unit star formation, sometimes called the SLSN production "efficiency."[22] Uncertainties are calculated using the method of Cameron (2011) (10%–90% confidence interval shown). A flat value of 1.0 would indicate a perfectly SF-tracing population.

The SN II production efficiency varies by no more than a factor of a few between galaxies of different mass ranges, none of which are significantly different from the uniform null hypothesis (relative efficiency of 1 in all bins), with the exception of the lowest-mass bin. Because the comparison survey is incomplete at the lowest stellar masses and our number statistics are limited, deviation in a single bin should not be overinterpreted, but it is intriguing that the two faintest galaxies in our overall sample are both hosts of SLSNe II (the host of Type II SN 2008es is similarly faint; Angus et al. 2016).

In contrast, the variation of the SLSN I production efficiency is enormous between galaxies of different masses, and the bulk of this variation occurs at moderate stellar masses. While the efficiency varies little between 10^6–$10^9 \, M_\odot$, it is a factor of 20 less than this in galaxies in the range of 10^{10}–$10^{11} \, M_\odot$. (Curiously, it then recovers in the $>10^{11} \, M_\odot$ bin, although this determination is based on only a single outlier event, PTF 10uhf.)

To better quantify this effect, we hypothesized that the SLSN I rate is constant in galaxies with stellar mass below some value M_{thresh} and nearly zero above the same value. To test this hypothesis and measure this value, we truncate the Ultra-VISTA sample above M_{thresh} and fit the truncated sample against our host mass distribution to find the optimum value of M_{thresh}; we derive a value of $1.6 \times 10^9 \, M_\odot$. (Curves corresponding to this model are shown in light gray in Figure 7). A K-S test between the truncated galaxy sample and the SLSNe I in our sample indicates that this model is a good fit ($p = 0.38$ of being drawn from the same distribution, although the K-S test tends to underweight the impact of extreme values: in this case, PTF 10uhf).

These observations seem to argue that the variation of the SLSN I efficiency is governed by suppression that operates among galaxies with masses above a few $\times 10^9 \, M_\odot$—preventing SLSN formation in these systems (except perhaps in unusual circumstances) but exerting little influence on the efficiency in lower-mass galaxies.

All of these conclusions are, of course, dependent on our sample not being subject to selection effects. It is possible that the absence of SLSNe in high-mass galaxies may in part be due to biases in targeting transients for spectral classification, although it is very unlikely that the magnitude of the SLSN I variation can be explained in this way. This will be discussed in more detail in Section 6.1.

5.4. SFRs and Specific Star Formation Rates

The sample displays a large range of star formation activity, ranging from $\sim 20 \, M_\odot \, \mathrm{yr}^{-1}$ all the way down to systems too faint for their star formation to be detected spectroscopically (a limit of typically $<0.1 \, M_\odot \, \mathrm{yr}^{-1}$; modeling of the SEDs suggest that the true values are $\sim 10^{-2} \, M_\odot \, \mathrm{yr}^{-1}$). SFR is strongly correlated with stellar mass in typical galaxies (with more massive galaxies producing proportionally more star formation), so the star formation properties of the sample are best interpreted by plotting SFR together with stellar mass

---

[21] Notably, however, the high-z Ultra-VISTA sample contains a small but significant contribution from very high mass ($>10^{11} \, M_\odot$) galaxies; in local samples the contribution from this range is essentially zero.

[22] Mathematically, the SLSN production efficiency ϵ can be defined as the number of SLSNe per unit time occurring in a cosmic volume divided by the SFR in the same volume: $\epsilon = R_{SN}/\mathrm{SFR}$. This can can refer to all galaxies within a true physical volume but more frequently is subdivided based on host parameters of interest. In this case we subdivide it by stellar mass: $\epsilon(M_*) = R_{SN}(M_*)/\mathrm{SFR}(M_*)$. Its absolute units are $M_\odot^{-1}$, but because the absolute SLSN rate is quite uncertain, we generally only deal with the normalized SLSN efficiency $\hat{\epsilon}$ in this paper; this is the efficiency in a particular stellar-mass bin divided by the average cosmic efficiency across all galaxies at similar redshift: $\hat{\epsilon}(M_*) = \epsilon(M_*)/\epsilon$. This is a unitless quantity and is what we have plotted in the bottom panel of Figure 7.

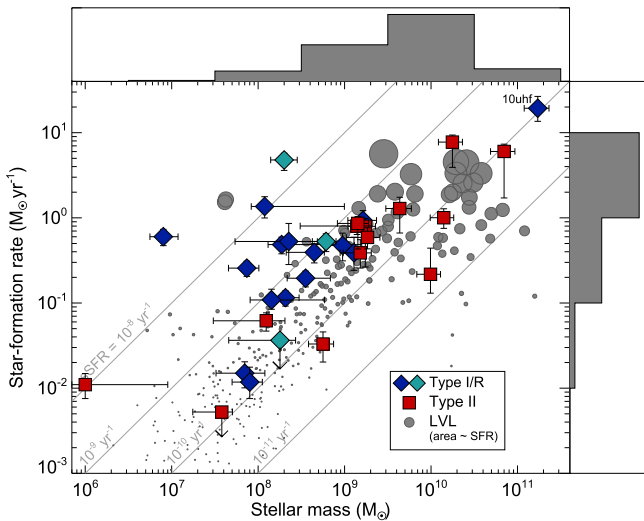**Figure 8.** SFRs and stellar masses of SLSN host galaxies from PTF compared to local galaxies from LVL. We employ the dust-corrected Hα SFRs where this line is detected, or otherwise fall back on the SED-derived average SFRs. Most galaxies (including most SLSN host galaxies) lie along the star-forming galaxy "main sequence" with a specific SFR between 10^{-10} and 10^{-9} yr^{-1}. SLSNe I (but not SLSNe II) are frequently found in galaxies that are forming stars much more rapidly than average for their mass ("starbursts"), although the majority are on the main sequence. The histograms on the top and right show the relative contributions of galaxies in LVL to the local SFR density as a function of the parameter on each axis (similar to the middle panel of Figure 7). Gray diagonals show lines of constant specific SFR.

(Figure 8). In this diagram we have also marked lines of constant *specific* SFR as diagonal lines.

Most of cosmic star formation, and indeed most SLSNe, occur in a relatively narrow region of the diagram with a specific SFR (sSFR $\equiv$ SFR$/M_*$), sSFR $= 10^{-9}$–10^{-10} yr^{-1}; this feature is a direct manifestation of the M_*–SFR correlation and is often referred to as the galaxy main sequence. We refer to galaxies significantly above the main sequence as "starbursts" since their rarity and mass-doubling/gas-consumption timescales imply that these are transient and short-lived phenomena; galaxies well below the main sequence are denoted as "quenched."

The high-mass portion of the main sequence is somewhat underpopulated by SLSNe (especially SLSNe I), as we have already noted in the previous section. The most interesting feature of this plot, however, is the presence of a significant fraction of our SLSNe I in extremely active starburst galaxies with SFRs 1–2 orders of magnitude in excess of the M_*–SFR correlation. Depending on the exact stellar masses of these objects (which can be difficult to measure because their light is dominated by the youngest stars), 3–6 SLSN I hosts (out of our sample of 18) and 0–2 SLSN II hosts (out of 13) are starbursts with sSFR $> 2 \times 10^{-9}$ yr^{-1}.

Galaxies of this type are rare cosmologically. Their true abundance (and contribution to the local SFR density) is difficult to estimate precisely, but (for example) only 5% of the star formation in the LVL sample occurs in galaxies with sSFR $>2 \times 10^{-9}$ yr^{-1} (see also Lee et al. 2009; similar values are reported from other surveys, e.g., Bergvall et al. 2016). Given the small sample sizes involved (in particular within LVL: the starburst–galaxy contribution to star formation within the local volume is driven by only two galaxies, NGC 1569 and II Zw 40), it is not clear that this trend is statistically significant, and
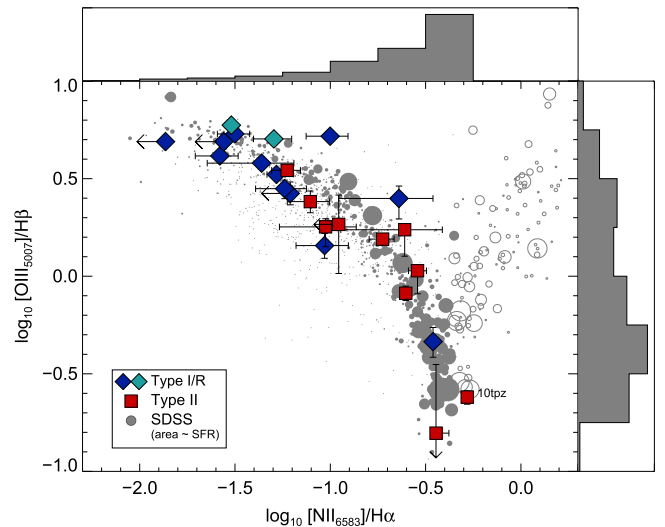
Figure 9. BPT diagram for SLSN hosts, compared to SDSS galaxies. AGNs within SDSS are identified via the criterion log([N II]/Hα) > -0.35 and are indicated as open circles. All SLSN hosts lie on the star-forming branch and closely follow the same narrow locus as SDSS star-forming galaxies (the host of PTF 10tpz shows evidence for an AGN contribution to the nuclear flux). Histograms along the *x*- and *y*-axes show the relative contribution from SDSS galaxies to the SFR density as a function of each parameter (as in Figure 8).

we cannot reliably provide an estimate for its quantitative magnitude in the way that we were able to measure the host-mass dependency of the SLSN rates. However, a similarly high or even higher starburst fraction was seen in the sample of Leloudas et al. (2015), so it is unlikely to be a statistical fluke of our sample; furthermore, it is *not* seen in ordinary SNe or even GRBs (Leloudas et al. 2011, 2015; Sanders et al. 2012), suggesting that it is not a limitation of the LVL volume or the result of redshift evolution.

This preference could, in principle, have the same physical origin as the preference toward low-mass galaxies: possibly, SLSNe prefer starburst galaxies simply because low-mass galaxies are more likely to be starbursts. (The reverse case can also be considered: SLSNe may prefer low-mass galaxies because only low-mass galaxies undergo starbursts at low *z*.) Distinguishing cause from effect in this case is difficult and requires, in particular, an accurate assessment of the starburst contribution to stellar-mass buildup in dwarf galaxies, which is quite uncertain (e.g., McQuinn et al. 2010). We will return to this question later in the discussion (Section 6.2).

5.5. Line Ratios

The BPT (Baldwin et al. 1981) diagram for our SLSN hosts and an SDSS comparison sample (Section 3.7.3) is shown in Figure 9. The usual bifurcation of star-forming and AGN branches is evident; all SLSN hosts lie on the star-forming branch (PTF 10tpz shows evidence for a subdominant contribution from an AGN). Indeed, the positions of the SLSN hosts are fully consistent with the locus of low-*z* galaxies; possible exceptions (PTF 10hgi and PTF 10vqv) differ only by $\sim2\sigma$. They therefore show no evidence of physically unusual environmental conditions (e.g., high-*T* stellar ionization field or unusual N/O ratio) relative to other low-*z* galaxies; in particular, they do not show the same offsets from the BPT
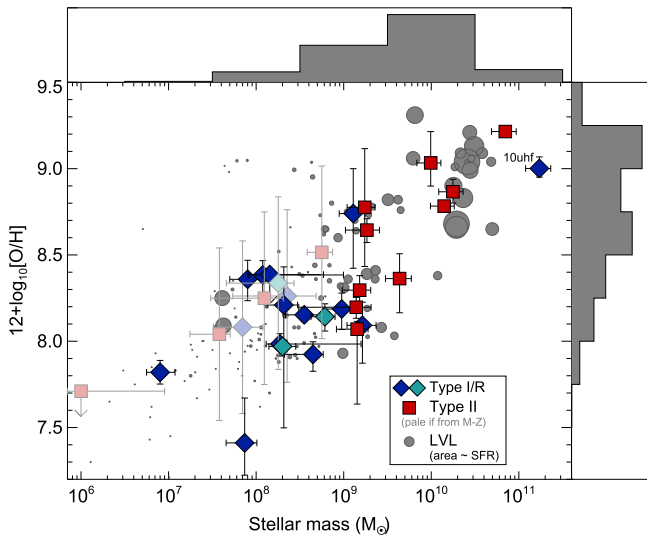
Figure 10. Mass–metallicity relation for SLSN hosts compared to LVL galaxies. SLSN hosts generally follow the mass–metallicity relation, allowing for the large intrinsic scatter in this relation (light-colored points have metallicities derived from the M–Z relation itself: either because no spectroscopic data were available, or because the emission lines were too weak to permit direct analysis). SLSNe I tend to inhabit galaxies with moderately low masses ($\sim 10^{8.5}\,M_\odot$) and metallicities ($12 + \log_{10}[\mathrm{O/H}] \approx 8.2$). Histograms are as in Figure 8.

diagram that have been inferred in high-redshift star-forming galaxies (e.g., Sanders et al. 2015). Nevertheless, as can be easily seen from the histogram subplots, there is favoritism for SLSNe toward the top left of the star-forming locus—the region dominated by low-metallicity galaxies.

5.6. Metallicity

In Figure 10 we plot the stellar mass versus our "best" estimate of the metallicity. Where [O III] $\lambda 4363$ is well detected, we employ T_e-based metallicities; if it is poorly detected or absent, we employ [N II]/Hα using the calibration of Nagao et al. 2006. (We emphasize, however, that our results do not depend significantly on the choice of calibration and similar results would be achieved using other diagnostics, and a table of metallicity diagnostics in various alternate calibration systems is presented in Table 6.) If even Hα is absent, we fall back on the metallicity predicted by the redshift-dependent mass–metallicity relation of Zahid et al. (2014), adjusted uniformly by -0.15 dex to better match the observed relation in LVL; we assume a large uncertainty of 0.5 dex on these values.[23]

While the vast spectroscopic coverage and high-quality data provided by SDSS would potentially make this survey ideal as a metallicity comparison sample in many ways, the fiber bias (Section 3.7.3) and possible star/galaxy classification biases introduce severe systematic problems. Accordingly, we fall back on the (small) LVL sample. While not every galaxy in this sample has a measured metallicity, the subset of galaxies with measurements appears to be representative of the sample as a whole: no biases are evident in mass, SFR, or other parameters.

We caution that the metallicity measurements of this sample (as compiled by Cook et al. 2014b) are compiled from the literature and use a variety of different diagnostics: typically T_e at low metallicities and various strong-line diagnostics at higher metallicities. While this general approach is the same as the one we employ for our SLSN host sample, the actual diagnostics employed are not always the same, introducing additional systematic uncertainty in our comparisons that should be kept in mind during the ensuing discussion.

Consistent with previous studies (Lunnan et al. 2014; Chen et al. 2015), we find that SLSNe I are highly underabundant in the most metal-rich galaxies. All but two occupy galaxies with metallicities[24] below $12 + \log_{10}[\mathrm{O/H}] \lesssim 8.5$, even though the majority of local star formation occurs at higher metallicities. Their metallicities, however, tend to not be *much* lower: all but one have values above 7.8, and the median value is 8.2 (1/3 solar). In addition, with or without the mass–metallicity-based values included, the position of the SLSN hosts in Figure 10 gives no indication of an offset relative to the local mass–metallicity relation. This suggests that the metallicity dependence of the SLSN I production efficiency follows similar qualitative behavior to the stellar-mass dependence: uniform at values below a critical threshold, above which the production efficiency drops precipitously.

Given the difficulty of establishing a complete comparison sample of star-forming galaxies using identical metallicity-measurement techniques as our host sample, it is difficult to measure this threshold precisely, but it must lie above the majority of our SLSN host metallicities ($12 + \log_{10}[\mathrm{O/H}] \gtrsim 8.2$–8.4) yet below the metallicities of "typical" spirals, which dominate the cosmic SFR density and are almost never found to host SLSNe ($12 + \log_{10}[\mathrm{O/H}] \lesssim 8.6$). A reasonable working hypothesis—to be tested and refined by future[25] studies—is that the SLSN efficiency is constant below half-solar ($12 + \log_{10}[\mathrm{O/H}] < 8.4$) and extremely low above this value.

6. DISCUSSION

6.1. Selection Biases?

It is of obvious importance to consider to what extent any of the results above might be influenced by selection effects. Biases can be intrinsic (due to extinction or source confusion/ blending preventing detection in the imaging survey) or extrinsic (due to follow-up/classification biases preventing recognition that some events present in the imaging survey are indeed SLSNe).

6.1.1. Extinction and Confusion

As SLSNe are always optically selected, extinction-related bias is unavoidable. It is probably not, however, particularly important in the case of our sample. First, most low-redshift galaxies are optically thin ($A_V < 1$ mag, as confirmed by the LVL extinction data); most star formation is not heavily obscured. Indeed, most optical surveys—including PTF itself

---

[23] While obviously the use of M–Z is nonoptimal and would be circular for evaluating the relative positions of SLSN hosts relative to the M–Z diagram, excluding these galaxies completely would bias our results since the galaxies with no Hα preferentially have low mass and low sSFR. Only seven of our metallicity values rely on the M–Z relation.

[24] These numbers refer to our "preferred" values combining the T_e and N06 metallicity scales, but equivalent results are obtained if any major scale is adopted. For example, if the KK04 scale is exclusively adopted, metallicities increase by about 0.1 dex in most of our galaxies, but all targets except for the host of PTF 10uhf remain below $12 + \log_{10}[\mathrm{O/H}] < 8.55$.

[25] We note that, following the initial submission of this paper, a 0.5 $Z_\odot$ metallicity cutoff for SLSN I production was independently proposed by Chen et al. (2016).

Table 6
Emission-line Diagnostics for SLSN Hosts

PTF ID	$SFR_{H\alpha}$ [a]	A_V [b]	12 + $\log_{10}$[O/H]											
			"Best"[c]	T_e	N06 N2	N06 R_{23}	D02	PP04 N2	PP04 O3	M08	M13 O3	M13 N2	KK04	KD02
09as	$0.485^{+0.108}_{-0.107}$	$0.64^{+0.12}_{-0.12}$	$7.98^{+0.05}_{-0.07}$	$7.88^{+0.17}_{-0.12}$	$7.98^{+0.05}_{-0.07}$	8.07	$8.04^{+0.17}_{-0.18}$	$8.08^{+0.03}_{-0.04}$	$8.02^{+0.02}_{-0.03}$	$8.10^{+0.06}_{-0.09}$	$8.06^{+0.02}_{-0.03}$	$8.05^{+0.06}_{-0.06}$	$8.10^{+0.06}_{-0.09}$	$8.10^{+0.06}_{-0.09}$
09uy	$0.796^{+0.188}_{-0.530}$	$2.00^{+0.07}_{-1.17}$	$8.78^{+0.34}_{-0.34}$	⋯	$8.78^{+0.34}_{-0.34}$	$8.07^{+0.59}$	$8.68^{+0.11}_{-0.19}$	$8.54^{+0.11}_{-0.17}$	$8.47^{+0.05}_{-0.09}$	$8.84^{+0.12}_{-0.19}$	$8.36^{+0.03}_{-0.06}$	$8.47^{+0.06}_{-0.12}$	$8.83^{+0.09}_{-0.16}$	$8.29^{+0.11}_{-0.26}$
09atu	<0.105	0	⋯	⋯	⋯	⋯	⋯	⋯	⋯	⋯	⋯	⋯	⋯	⋯
09cnd	$0.115^{+0.023}_{-0.023}$	0	$8.21^{+0.22}_{-0.71}$	⋯	$8.21^{+0.22}_{-0.71}$	$8.63^{+0.04}_{-1.18}$	$8.27^{+0.19}_{-0.31}$	$8.22^{+0.09}_{-0.15}$	$8.23^{+0.06}_{-0.13}$	$8.43^{+0.22}_{-0.32}$	$8.19^{+0.05}_{-0.09}$	$8.21^{+0.10}_{-0.19}$	$8.42^{+0.17}_{-0.38}$	$8.24^{+0.16}_{-0.43}$
09cwl	<0.061	0	⋯	⋯	⋯	⋯	⋯	⋯	⋯	⋯	⋯	⋯	⋯	⋯
10bfz	$0.393^{+0.104}_{-0.097}$	$0.32^{+0.21}_{-0.20}$	$7.92^{+0.07}_{-0.09}$	$7.75^{+0.17}_{-0.14}$	$7.92^{+0.07}_{-0.09}$	$7.69^{+0.10}_{-0.07}$	$7.96^{+0.18}_{-0.19}$	$8.04^{+0.04}_{-0.06}$	$8.03^{+0.04}_{-0.04}$	$8.02^{+0.09}_{-0.12}$	$8.06^{+0.03}_{-0.03}$	$8.01^{+0.06}_{-0.08}$	$8.02^{+0.10}_{-0.12}$	$8.02^{+0.10}_{-0.12}$
10bjp	$0.934^{+0.283}_{-0.254}$	$0.38^{+0.26}_{-0.27}$	$8.09^{+0.13}_{-0.21}$	⋯	$8.09^{+0.13}_{-0.21}$	$7.77^{+0.64}_{-0.07}$	$8.14^{+0.17}_{-0.23}$	$8.14^{+0.06}_{-0.10}$	$8.12^{+0.05}_{-0.09}$	$8.24^{+0.13}_{-0.23}$	$8.12^{+0.04}_{-0.06}$	$8.12^{+0.09}_{-0.12}$	$8.25^{+0.14}_{-0.24}$	$8.24^{+0.13}_{-0.25}$
10cwr	$0.257^{+0.052}_{-0.051}$	<0.04	$7.41^{+0.26}_{-0.18}$	$7.41^{+0.26}_{-0.18}$	$7.67^{+0.27}_{-7.67}$	$7.76^{+0.20}_{-0.10}$	$7.82^{+0.25}_{-0.39}$	$7.96^{+0.12}_{-0.24}$	$7.94^{+0.09}_{-0.14}$	$7.94^{+0.75}_{-0.39}$	$8.01^{+0.06}_{-0.10}$	$7.92^{+0.14}_{-0.20}$	$7.82^{+0.26}_{-0.61}$	$7.82^{+0.26}_{-0.61}$
10fel	$1.003^{+0.274}_{-0.250}$	$0.85^{+0.22}_{-0.21}$	$8.78^{+0.02}_{-0.02}$	⋯	$8.78^{+0.02}_{-0.02}$	$8.86^{+0.05}_{-0.05}$	$8.09^{+0.25}_{-0.54}$	$8.08^{+0.14}_{-0.13}$	$8.22^{+0.12}_{-0.26}$	8.69	$8.20^{+0.08}_{-0.19}$	$8.07^{+0.14}_{-0.41}$	$8.08^{+0.32}_{-1.15}$	$8.06^{+0.24}_{-1.20}$
10heh	$0.387^{+0.166}_{-0.130}$	$0.82^{+0.38}_{-0.39}$	$8.30^{+0.08}_{-0.09}$	⋯	$8.30^{+0.08}_{-0.09}$	$8.46^{+0.14}_{-0.38}$	$8.30^{+0.14}_{-0.14}$	$8.23^{+0.03}_{-0.04}$	$8.26^{+0.02}_{-0.03}$	$8.43^{+0.05}_{-0.08}$	$8.22^{+0.02}_{-0.02}$	$8.23^{+0.05}_{-0.06}$	$8.46^{+0.06}_{-0.08}$	$8.41^{+0.04}_{-0.09}$
10hgi	$0.012^{+0.005}_{-0.004}$	$0.88^{+0.46}_{-0.41}$	$8.36^{+0.11}_{-0.12}$	⋯	$8.36^{+0.11}_{-0.12}$	$9.13^{+0.04}_{-0.05}$	$8.37^{+0.14}_{-0.17}$	$8.27^{+0.05}_{-0.06}$	$8.36^{+0.03}_{-0.05}$	$8.49^{+0.08}_{-0.12}$	$8.28^{+0.02}_{-0.03}$	$8.26^{+0.06}_{-0.07}$	$8.52^{+0.08}_{-0.13}$	$8.38^{+0.06}_{-0.12}$
10jwd	$7.750^{+1.633}_{-3.833}$	$2.89_{-0.78}$	$8.87^{+0.07}_{-0.06}$	⋯	$8.87^{+0.07}_{-0.06}$	$8.07^{+0.44}$	$8.72^{+0.09}_{-0.08}$	$8.59^{+0.03}_{-0.03}$	$8.56^{+0.01}_{-0.02}$	$8.90^{+0.03}_{-0.03}$	$8.42^{+0.01}_{-0.01}$	$8.49^{+0.03}_{-0.03}$	$8.87^{+0.02}_{-0.02}$	⋯
10nmn	$0.528^{+0.121}_{-0.126}$	$1.21^{+0.13}_{-0.18}$	$8.14^{+0.07}_{-0.08}$	⋯	$8.14^{+0.07}_{-0.08}$	8.07	$8.17^{+0.15}_{-0.16}$	$8.16^{+0.03}_{-0.04}$	$8.10^{+0.03}_{-0.04}$	$8.27^{+0.07}_{-0.09}$	$8.11^{+0.02}_{-0.03}$	$8.14^{+0.05}_{-0.06}$	$8.28^{+0.08}_{-0.09}$	$8.28^{+0.07}_{-0.09}$
10qaf	$1.287^{+0.456}_{-0.623}$	$1.29^{+0.32}_{-0.77}$	$8.36^{+0.14}_{-0.19}$	⋯	$8.36^{+0.14}_{-0.19}$	$8.41^{+0.28}_{-0.33}$	$8.36^{+0.15}_{-0.20}$	$8.27^{+0.07}_{-0.09}$	$8.33^{+0.05}_{-0.08}$	$8.49^{+0.10}_{-0.17}$	$8.26^{+0.04}_{-0.05}$	$8.27^{+0.07}_{-0.11}$	$8.53^{+0.11}_{-0.19}$	$8.35^{+0.08}_{-0.21}$
10qwu	$0.062^{+0.014}_{-0.015}$	<0.70	⋯	⋯	⋯	⋯	$8.47^{+0.19}_{-0.28}$	$8.35^{+0.13}_{-0.16}$	$8.37^{+0.08}_{-0.14}$	$8.67^{+0.06}_{-0.28}$	$8.29^{+0.05}_{-0.09}$	$8.34^{+0.10}_{-0.16}$	$8.65^{+0.14}_{-0.30}$	$8.30^{+0.12}_{-0.46}$
10scc	<0.047	0	⋯	⋯	⋯	⋯	⋯	⋯	⋯	⋯	⋯	⋯	⋯	⋯
10tpz	$6.020^{+1.310}_{-1.298}$	$2.31^{+0.09}_{-0.09}$	9.22	⋯	9.22	$9.16^{+0.01}_{-0.01}$	$8.92^{+0.05}_{-0.06}$	8.86	$8.85^{+0.01}_{-0.01}$	$8.61^{+0.02}_{-0.03}$	$8.61^{+0.03}_{-0.03}$	$9.16^{+0.01}_{-0.01}$	⋯	⋯
10uhf	$19.36^{+7.301}_{-5.764}$	$1.75^{+0.34}_{-0.32}$	$9.00^{+0.06}_{-0.05}$	⋯	$9.00^{+0.06}_{-0.05}$	$8.94^{+0.06}_{-0.07}$	$8.79^{+0.07}_{-0.07}$	$8.67^{+0.01}_{-0.01}$	$8.70^{+0.01}_{-0.01}$	$8.98^{+0.01}_{-0.01}$	$8.51^{+0.01}_{-0.01}$	$8.53^{+0.03}_{-0.03}$	$8.93^{+0.01}_{-0.01}$	⋯
10vqv	$1.360^{+0.410}_{-0.363}$	$0.31^{+0.25}_{-0.24}$	$8.38^{+0.08}_{-0.10}$	⋯	$8.38^{+0.08}_{-0.10}$	$8.20^{+0.15}_{-0.13}$	$8.39^{+0.12}_{-0.14}$	$8.28^{+0.04}_{-0.05}$	$8.18^{+0.03}_{-0.04}$	$8.51^{+0.06}_{-0.08}$	$8.16^{+0.02}_{-0.03}$	$8.28^{+0.05}_{-0.06}$	$8.55^{+0.06}_{-0.09}$	$8.42^{+0.03}_{-0.08}$
10vwg	<0.072	0	⋯	⋯	⋯	⋯	⋯	⋯	⋯	⋯	⋯	⋯	⋯	⋯
10yyc	$0.218^{+0.223}_{-0.087}$	$0.57^{+0.90}_{-0.57}$	$9.03^{+0.18}_{-0.13}$	⋯	$9.03^{+0.18}_{-0.13}$	$9.30^{+0.08}_{-0.18}$	$8.79^{+0.07}_{-0.07}$	$8.69^{+0.05}_{-0.05}$	$8.81^{+0.12}_{-0.05}$	$9.00^{+0.05}_{-0.04}$	$8.59^{+0.09}_{-0.03}$	$8.54^{+0.03}_{-0.03}$	$8.95^{+0.04}_{-0.04}$	⋯
10aagc	$0.474^{+0.187}_{-0.160}$	$0.45^{+0.37}_{-0.42}$	$8.19^{+0.09}_{-0.11}$	⋯	$8.19^{+0.09}_{-0.11}$	$8.48^{+0.12}_{-0.72}$	$8.21^{+0.16}_{-0.17}$	$8.18^{+0.04}_{-0.05}$	$8.19^{+0.04}_{-0.05}$	$8.33^{+0.08}_{-0.12}$	$8.18^{+0.03}_{-0.04}$	$8.17^{+0.06}_{-0.08}$	$8.35^{+0.09}_{-0.13}$	$8.34^{+0.07}_{-0.14}$
11dij	$0.600^{+0.132}_{-0.129}$	$0.63^{+0.11}_{-0.10}$	$7.82^{+0.06}_{-0.06}$	$7.82^{+0.06}_{-0.06}$	$7.71^{+0.15}_{-0.43}$	$7.82^{+0.06}_{-0.05}$	$7.76^{+0.25}_{-0.32}$	$7.93^{+0.10}_{-0.20}$	$7.93^{+0.06}_{-0.10}$	$7.80^{+0.21}_{-0.29}$	$7.99^{+0.05}_{-0.07}$	$7.90^{+0.10}_{-0.16}$	$7.76^{+0.21}_{-0.45}$	$7.76^{+0.21}_{-0.45}$
11dsf	$0.802^{+0.195}_{-0.164}$	$0.04^{+0.15}_{-0.04}$	$8.20^{+0.05}_{-0.06}$	⋯	$8.20^{+0.05}_{-0.06}$	$8.52^{+0.03}_{-0.06}$	$8.22^{+0.15}_{-0.14}$	$8.18^{+0.02}_{-0.03}$	$8.16^{+0.02}_{-0.03}$	$8.33^{+0.05}_{-0.06}$	$8.15^{+0.02}_{-0.02}$	$8.17^{+0.05}_{-0.05}$	$8.35^{+0.06}_{-0.07}$	$8.35^{+0.05}_{-0.07}$
11hrq	$0.196^{+0.040}_{-0.040}$	$0.29^{+0.07}_{-0.07}$	$8.15^{+0.03}_{-0.03}$	$8.25^{+0.25}_{-0.17}$	$8.15^{+0.03}_{-0.03}$	$8.43^{+0.05}_{-0.05}$	$8.19^{+0.14}_{-0.14}$	$8.16^{+0.01}_{-0.02}$	$8.15^{+0.01}_{-0.01}$	$8.28^{+0.03}_{-0.04}$	$8.15^{+0.01}_{-0.01}$	$8.15^{+0.04}_{-0.05}$	$8.30^{+0.03}_{-0.04}$	$8.30^{+0.03}_{-0.04}$
11rks	$0.389^{+0.202}_{-0.147}$	$0.46^{+0.49}_{-0.46}$	$8.74^{+0.26}_{-0.31}$	⋯	$8.74^{+0.26}_{-0.31}$	$8.53^{+0.19}_{-0.46}$	$8.13^{+0.25}_{-0.38}$	$8.14^{+0.13}_{-0.18}$	$8.17^{+0.11}_{-0.17}$	$8.69_{-0.40}$	$8.16^{+0.08}_{-0.11}$	$8.13^{+0.14}_{-0.22}$	$8.24^{+0.29}_{-0.50}$	$8.12^{+0.23}_{-0.51}$
12dam	$4.781^{+0.956}_{-1.174}$	$0.25_{-0.20}$	$7.97^{+0.02}_{-0.02}$	$8.09^{+0.03}_{-0.05}$	$7.97^{+0.02}_{-0.02}$	8.07	$8.00^{+0.16}_{-0.15}$	$8.07^{+0.01}_{-0.01}$	$8.00^{+0.01}_{-0.01}$	$8.08^{+0.02}_{-0.03}$	$8.04^{+0.02}_{-0.02}$	$8.04^{+0.04}_{-0.05}$	$8.08^{+0.02}_{-0.03}$	$8.08^{+0.02}_{-0.03}$
12epg	$0.589^{+0.174}_{-0.156}$	$0.62^{+0.21}_{-0.20}$	$8.64^{+0.06}_{-0.07}$	⋯	$8.64^{+0.06}_{-0.07}$	$8.65^{+0.04}_{-0.05}$	$8.59^{+0.09}_{-0.09}$	$8.44^{+0.03}_{-0.04}$	$8.44^{+0.01}_{-0.02}$	$8.73^{+0.03}_{-0.04}$	$8.34^{+0.01}_{-0.01}$	$8.41^{+0.04}_{-0.04}$	$8.75^{+0.03}_{-0.04}$	⋯
12gwu	<0.013	0	⋯	⋯	⋯	⋯	⋯	⋯	⋯	⋯	⋯	⋯	⋯	⋯
12mkp	<0.010	0	⋯	⋯	⋯	⋯	⋯	⋯	⋯	⋯	⋯	⋯	⋯	⋯
12mue	$0.860^{+0.176}_{-0.429}$	$1.38^{+0.04}_{-0.79}$	$8.07^{+0.04}_{-0.43}$	⋯	<8.11	$8.07_{-0.43}$	$7.91^{+0.31}_{-0.40}$	$8.04^{+0.11}_{-0.32}$	$8.05^{+0.10}_{-0.17}$	$8.69_{-0.65}$	$8.07^{+0.07}_{-0.11}$	$7.99^{+0.15}_{-0.23}$	$7.99^{+0.28}_{-0.65}$	$7.98^{+0.28}_{-0.65}$
12mxx	$0.109^{+0.036}_{-0.024}$	<0.26	<8.38	⋯	<8.38	$6.95^{+2.08}_{-0.10}$	$8.25^{+0.22}_{-0.43}$	$8.19^{+0.13}_{-0.19}$	$8.35^{+0.10}_{-0.17}$	$8.69_{-0.46}$	$8.28^{+0.06}_{-0.11}$	$8.18^{+0.14}_{-0.24}$	$8.35^{+0.26}_{-0.50}$	$8.15^{+0.21}_{-0.61}$

Notes.
[a] Dust-corrected Hα SFR, in $M_\odot$ yr^{-1}.
[b] Balmer-decrement dust extinction, in mag.
[c] The "best" metallicity (the value presented in plots and elsewhere in the discussion) is the T_e metallicity when a high-significance detection of the [O III] λ4363 auroral line is available, or else the N06 (N2Hα) metallicity if [N II] is detected. The mass–metallicity relation is used if neither of these lines is detected.

(This table is available in machine-readable form.)

—have no difficulty finding other types of SNe in massive galaxies (see, e.g., Arcavi et al. 2010 for the luminosity distribution of the PTF core-collapse sample, and our discussion in the following section). Furthermore, if extinction were a major factor, we would expect its impact to be strongly dependent on redshift: SLSNe at $z \approx 0.1$ could be found relatively easily even behind 1–2 mag of extinction, whereas those at $z \approx 0.4$ would be affected most strongly. However, the lack of massive galaxies in the SLSN sample is evident at low redshifts as well as at high redshifts (Figure 6). Furthermore, an extinction effect would not explain the apparent differences between the host populations of SLSNe I and SLSNe II.

Source confusion is even less likely to be an issue, at least for the sample as a whole: PTF subtractions are generally quite clean except around the centers of massive nearby galaxies (which contribute little to star formation). Confusion-related biases could, however, conceal a population that occurs preferentially or exclusively in these environments. This may indeed be relevant in the case of PTF 10tpz, but it has no impact on the remainder of our sample.

6.1.2. Spectroscopic Follow-up Biases

A much more significant consideration is related to the fact that only a minority of PTF transients can be followed up and classified. While careful reanalysis of archival data suggests that the identification of transient candidates by scanners is highly complete and not biased (C. Frohmaier et al. 2016, in preparation), the manner in which candidates are chosen for spectroscopic follow-up is not uniform and heavily depends on human-based decision-making using information available around the time of discovery (Section 2.2). These decisions may include the apparent properties of the host in pre-imaging in some cases. Indeed, transients in faint/dwarf-like hosts and transients with no apparent host in pre-imaging are often explicitly flagged as interesting relative to transients within large and resolved intermediate-redshift ($z \approx 0.1$–0.2) galaxies, since the large majority of transients within the latter type of galaxy are SNe Ia (which, because of their numbers, are not usually emphasized for follow-up unless they are discovered very early or occur very nearby).

An approximate accounting for this effect can be measured by examining the host-galaxy sample for general PTF core-collapse SNe compiled by Arcavi et al. (2010). These SN hosts exhibit a median absolute magnitude of $M_r = -20$, with only a small fraction (19%) found within "dwarf" (<-18 mag) galaxies. This is, in fact, quite similar to the fraction of cosmic SFR occurring within galaxies of this absolute magnitude range (23%, for Ultra-VISTA galaxies at $z \approx 0.12$) and suggests that, at least in the first few years of PTF, galaxy-related classification biases did not have a large impact.

In addition to possible biases in *obtaining* spectroscopic follow-up, there may be biases in *interpreting* spectroscopic follow-up if transients within certain types of galaxies are easier to classify. For example, faint galaxies might contaminate the transient spectra less and make their features easier to recognize (this would lead to a bias against luminous galaxies), or underlying emission lines might reveal the redshift and therefore reveal that the transient is "superluminous" more readily (this would lead to a bias in favor of galaxies with strong emission lines).

We do not think that these possible biases are significant in our sample. SLSNe are comparable in brightness to even the most luminous galaxies, and it is very difficult to conceal their intrinsic features regardless of galaxy luminosity or type. In addition, at all but the lowest redshifts the UV absorption features that emerge in SLSN I post-peak are very clear and distinctive; furthermore, a careful late-time reanalysis of the entire PTF spectral database (R. Quimby et al. 2016, in preparation) identified only a single misclassified SLSN I, and we have included this event (PTF 09as) in our sample. The redshifts of SLSNe II are even more immediately apparent at the time of the first spectrum thanks to their narrow Balmer-series emission lines, although on the other hand it is conceivable that some SLSNe II with spectra might be missing from our sample due to misclassification as luminous AGNs/QSOs (which could bias SLSNe II against pointlike galaxies or small nuclear offsets).

Based on these arguments, we conclude that the trends evident in the PTF SLSN I sample above are genuine and reflect a true, intrinsic increase in likelihood of these events in low-mass, low-metallicity, high-sSFR galaxies. In the case of SLSNe II, our conclusion that they differ from the properties of general star-forming galaxies was only weakly significant in the first place, and it is conceivable that this trend could be erased once some of the selection effects above are considered. For these reasons, in the rest of the discussion we will focus primarily on the SLSN I population.

6.2. What Drives the SLSN I Rate Variation: Metallicity, Starbursts, Both, or Neither?

We previously (Section 5) noted two strong trends evident in the SLSN I host population. First, SLSNe I are very uncommon in galaxies with high masses and metallicities ($M_* > 10^{9.5} M_\odot$ and $Z > 0.5 Z_\odot$, respectively)—which could be interpreted as evidence for a metallicity-dependent progenitor mechanism. Second, they are remarkably common in "starburst" galaxies with high specific SFRs (sSFR $>10^{-9}$ yr^{-1})—which could be interpreted as evidence for a progenitor favored by an altered (e.g., top-heavy) IMF or dense clusters with abundant dynamical interactions. Is this evidence that *both* metallicity *and* an IMF/interactions contribute to producing SLSN progenitors?

Caution is warranted on this point: low-mass (low-metallicity) galaxies have burstier star formation histories than high-mass (high-metallicity) galaxies (e.g., Lee et al. 2009), and when starbursts do occur, they can be much more intense in dwarf galaxies. Furthermore, galaxies mid-starburst may exhibit lower gas-phase metallicities even when compared to others of the same mass (Mannucci et al. 2010). Given these influences, the simultaneous observation of both of the *observational* trends we highlight above is to some degree expected *even if* only one effect is operating—simply because the parameters correlate.

Because of the much greater strength of the metallicity trend (most star formation is metal-rich, most of our hosts are metal-poor) compared to the sSFR trend (most star formation is in nonstarbursts, and indeed most of our hosts are also nonstarbursts), it is more likely that a metallicity effect would be driving the starburst trend rather than vice versa. However, we can test this more directly by taking advantage of the fact that the correlations between galaxy parameters are not perfect ones, and examine the role of both factors simultaneously in a two-dimensional parameter space.
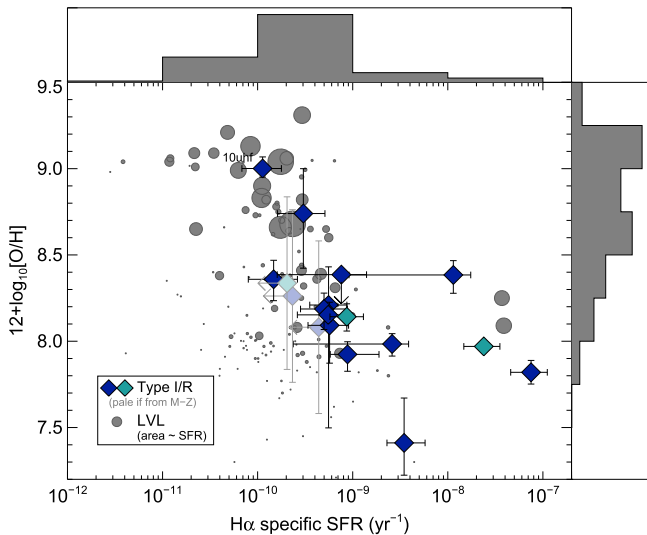
Figure 11. Specific SFR vs. metallicity. This plot can be used to help distinguish whether metallicity or star formation intensity is primarily responsible for the unusual properties of the SLSN I host population: a dominant metallicity effect would be seen as a concentration in the vertical direction relative to LVL galaxies, while a dominant SFR-intensity effect would be seen as a concentration in the horizontal direction. Many of the sSFR measurements are upper limits due to nondetection of Hα. SLSNe I clearly avoid metal-rich galaxies and may prefer somewhat elevated sSFRs compared to the LVL sample but do not require high sSFR. The three "extreme" SLSN I hosts in the right part of the figure (PTF 10vqv, PTF 11dij, and PTF 12dam) have few equivalents among local-volume galaxies. Histograms are as in Figure 8.

In Figure 11 we plot the two competing parameters (Z and sSFR) against each other directly, along with LVL galaxies with measured metallicities. SLSNe II are omitted for clarity. If metallicity is the dominant effect driving SLSN production, the hosts would preferentially avoid the top part of the diagram and cluster toward the middle and bottom, but their horizontal distribution would match local star formation within that space. If starburst intensity is a critical factor, SLSNe would preferentially occur toward the right side of the diagram relative to star-forming galaxies of the same metallicity.

We can rule out that the starburst trend *drives* the metallicity trend: even if starburst galaxies are removed, most of the hosts remain quite metal-poor compared to the majority of star formation in the local volume. It is less clear whether the reverse is also true (that is, whether a preference for starbursts remains if only the most metal-poor galaxies are considered). The three SLSN host galaxies that are strongly starbursting (PTF 10vqv, PTF 11dij, PTF 12dam) are also definitively metal-poor. In our local-volume comparison sample, the two most dramatic local-volume starbursts have comparable sSFRs to our three SLSN starburst hosts, but all three SLSNe I starbursts are poorer in metals—providing at least some suggestion that metallicity is the driving factor even in the high-sSFR regime. However, with sample sizes of only three hosts and two comparison galaxies, this statement has almost no statistical significance, and further studies of larger samples will be needed to evaluate this more definitively.

An alternative means of addressing this point would be to examine the precise spatial positions of the SLSNe *within* their hosts, especially for the starburst galaxies, to determine whether or not the SLSNe are indeed occuring in regions of the most intense star formation. This has been done previously by Lunnan et al. (2015) on a higher-redshift sample; they find

that SLSNe may slightly concentrate toward the brightest pixels but that this trend is not statistically significant. One of their events is a starburst galaxy in our sample (PTF 11dij/ SN 2011ke), and the SN appears on a pixel with a UV surface brightness higher than 86% of the remainder of the galaxy. In our own imaging of PTF 12dam, the SLSN sits on the brightest pixel of the F225W UV image (A. De Cia et al. 2016, in preparation). This may suggest that *very* high star formation volume densities may amplify the SLSN rate independent of metallicity, but that this effect drops away at ordinary SFR densities. We will need more UV imaging of the starburst subset of the SLSN I host population to confirm this possibility.

6.3. The Peculiar Hosts of PTF 10uhf and PTF 10tpz

The host galaxy of PTF 10uhf stands as a stark exception to many of the trends seen in the rest of the SLSN I host sample. It is massive, is metal-rich, and has a large population of evolved stars. Because the SN occurred far in the outer regions of this galaxy (possibly in a merging, dwarf companion), it is natural to appeal to the possibility of metallicity gradients to explain this peculiar case under the "maximum-metallicity" hypothesis we propose (Section 5.6). However, analysis of spectroscopy taken at the SN site shows no significant difference between this region and the rest of the host: the metallicity at the SN site is still well above our proposed threshold. Possibly, small-spatial-scale chemical inhomogeneities (Niino 2011) could conceal some low-metallicity star formation, although given the weakness of the [O III] line, this would have to represent a small fraction of the overall total. Alternatively, this host may provide evidence that SLSNe I are not completely suppressed in metal-rich environments: they may still occur at high Z, but at a much lower frequency.

Curiously, however, this host is at the extremes not only of the SLSN host population but also of the general galaxy population. If in principle an SLSN I can occur in any star-forming galaxy (due to chemical inhomogeneities, incomplete suppression at high metallicity, or other reasons), it is peculiar that the only metal-rich SLSN I in our sample happened to occur in one of the most luminous galaxies in the low-redshift universe. We might wonder, then, whether something exceptional about this galaxy might have enabled it to produce this event in a metallicity regime that would stifle the production of SLSNe in most other galaxies: perhaps the metallicity limit might be "lifted" in regions of the most vigorous star formation owing to an altered IMF. This specific explanation is not particularly natural either: star formation at the SN site, while clearly present, is not particularly vigorous (in terms of, e.g., [O III]/[O II] or Hα equivalent width). However, it is possible that there are other unusual physical attributes of the host and/ or the SN site that are less apparent.

With only a single example it is not possible to rule out any of these scenarios: the seemingly exceptional nature of its host could simply be a low-probability event, and future "high-metallicity" SLSNe will be found in more normal galaxies. Selection biases within PTF, while minor (Section 6.1), may also play a role. In any case, the occurrence of rare but dramatic outliers of this type clearly indicates the need to continue collecting large samples of SLSNe and their hosts to determine just how frequently the cosmos sees fit to violate the "rules" we might otherwise infer from smaller samples.

Indeed, our discovery of PTF 10tpz (an SLSN II) provides a possible illustration, showing that the very peculiar

environment of SN 2006gy (the circumnuclear regions of a massive and metal-rich galaxy) was probably *not* a fluke. Heavy obscuration and confusion limit the effective search volume for heavily obscured circumnuclear events of this type within PTF to a volume much smaller (by $\gtrsim 2$ orders of magnitude) than for unobscured SNe. Accounting for this, obscured circumnuclear SLSNe may in fact constitute the most common variety of SLSN. This is especially notable considering that the contribution to cosmic star formation from massive galaxy nuclei is miniscule. Low metallicity clearly is not the factor in this case, suggesting that—in the case of circumnuclear SLSNe II—a genuinely different factor is at play, such as a top-heavy IMF in galaxy nuclei. The presence of a central AGN in the host galaxies of both SN 2006gy and PTF 10tpz provides some evidence that the AGN itself may play a major role in shaping the nuclear star-forming environment.

Alternatively, it may be worth considering whether—despite being clearly located away from their host nuclei and exhibiting SN-like photometric and spectroscopic evolution—SN 2006gy and PTF 10tpz may not represent genuine SNe after all, but rather flares associated with a *second* supermassive black hole originating from a former companion galaxy that merged with the host in the recent past. The host of PTF 10tpz does indeed show some suggestions of a past merger in the form of two nonaligned disks (Figure 1). A detailed examination of this hypothesis will be reserved for future work.

6.4. Implications of a Metallicity Threshold for the SLSN I Progenitor

The roughly half-solar metallicity threshold for SLSN I production that we propose[26] poses a broad challenge to theoretical models for SLSN production. While an SLSN rate that depends strongly on metallicity is a natural prediction under a variety of scenarios, most of these suggest a critical threshold that is much lower ($\sim 0.1\,Z_\odot$, or even less)—or, at least, a smoother dependence in which the rate at very low metallicities is significantly higher than the rate at moderate metallicities.

Classical pair-instability models, including the pulsational pair-instability variant, suggested that only extremely low metallicity stars should explode as PISNe (e.g., Heger et al. 2003; Langer et al. 2007). Our observations would therefore seem to rule out this model for SLSNe I, including the slowly declining "R" subclass. However, more recent theoretical work suggests that the picture is more equivocal: for example, Yusof et al. (2013) are able to produce pair-instability explosions at up to $Z \approx 0.5\,Z_\odot$ (see also Marchant et al. 2016). However, these studies also predict that the rate at very low metallicities should be much higher than at $Z \sim 0.5 Z_\odot$, contrary to our observations. While individual SLSNe in our sample may remain viably explained by PISNe, it remains unclear why we do not find more examples in galaxies that are (even) lower in mass and metallicity than those in our sample.

Explaining a relatively high metallicity "threshold" in the SLSN I efficiency is challenging for other models as well, although the wider range of evolutionary pathways and initial masses available to both the magnetar model and core-collapse +interaction model (especially when binary evolution is

---

[26] As we measure only galaxy-averaged metallicities, it is possible that the true metallicities at the progenitor site are somewhat lower than our reported values (Niino 2011). However, they are unlikely to be dramatically lower as an ensemble, especially considering the small physical sizes of most of our objects.

considered) may offer some additional flexibility. Interestingly, this problem is shared with GRBs, whose rate dependence on metallicity seems to exhibit at least qualitatively similar behavior to what we report here for SLSNe (Krühler et al. 2015; Vergani et al. 2015; Perley et al. 2016).

Whatever the underlying reason, this similar behavior provides some evidence for a close connection between the progenitors of SLSNe I and GRBs—and since the progenitor of GRBs is almost certainly *not* supermassive given the much lower typical luminosities and ejecta masses of the SNe accompanying GRBs, this might argue that a central-engine model (which almost certainly explains GRBs) applies for SLSNe I also (Lunnan et al. 2014).

On the other hand, the inferred metallicity threshold for GRBs from the studies above ($\sim 1.0\,Z_\odot$) is significantly higher than what we measured for SLSNe I in this work ($\sim 0.5\,Z_\odot$). These studies were conducted at different redshift ranges and (in some cases) using different techniques, and until a large, complete comparison sample of SLSNe and GRBs at similar redshifts is available, we should exercise caution in comparing their environmental preferences directly. Nevertheless, other forms of evidence also suggest that the host environments of GRBs and SLSNe I do in fact differ (Vreeswijk et al. 2014; Leloudas et al. 2015; Angus et al. 2016; see also the low-z subset of Lunnan et al. 2014). Further studies of both populations will be needed to confirm that these differences are intrinsic and significant, and genuine differences between the GRB and SLSN host populations may indeed be present even if they share a common central engine (clearly, the very different nature of these events requires *some* differences in their formation histories). In any case, we cannot yet argue that the similiarities between SLSN and GRB hosts establish a clear connection between their progenitors or energy sources.

The least exotic progenitor model—an "ordinary" but high-mass core-collapse explosion interacting with a massive hydrogen-poor envelope—is perhaps the most difficult to rule out since it requires neither rapid rotation nor an extremely large core mass, establishing fewer constraints on its evolutionary pathway before explosion.

6.5. Constraints from Young Starburst Ages on the SLSN I Progenitor Mass

In cases where a host galaxy is undergoing a particularly young and active starburst, its properties can be used more directly to constrain the nature of the progenitor. It is reasonable to assume in these cases that the progenitor was formed during the starburst episode and that its lifetime cannot be longer than that of the starburst itself, placing a maximum age on the progenitor that can be translated to a minimum initial mass. Only quite extreme galaxies are capable of providing a meaningful constraint: any star large enough to explain the ejecta masses inferred from typical SLSNe will have an initial mass well exceeding $20\,M_\odot$ and a lifetime shorter than 10 Myr, so galaxies undergoing starbursts older than this provide no additional information about the progenitor age. Fortunately, a few SLSN hosts are indeed quite extreme. The host of PTF 12dam is the best-studied example; a high-S/N spectrum of this galaxy has been previously used by Thöne et al. (2015) to conclude that the starburst age was ~ 2 Myr, corresponding to an initial progenitor mass of $> 60\,M_\odot$. The host of PTF 11dij is even more extreme in its color and equivalent widths, and we

suggest that more detailed modeling of this event may be able to place even more stringent constraints on the initial mass range of its progenitor. Very massive progenitors are required in the PISN and interacting CCSN models, but lower-mass progenitors are more likely under the magnetar model, so these observations may therefore argue in favor of one of the former two cases.

However, we caution against attempts to generalize these conclusions to the entire sample: while their extreme properties attract attention, hosts like PTF 12dam and PTF 11dij represent a small minority of the population, and the sSFRs of most of our hosts (including the other starbursts) correspond to characteristic ages of 100 Myr or more. This is not necessarily problematic for an ultramassive progenitor star (such stars are expected to form outside young starbursts as well). On the other hand, the resolved *HST* analysis of Lunnan et al. (2015) shows no clear tendency for SLSNe to prefer the most UV-luminous portions within their host galaxies, as would be expected if their progenitor was exclusively very short-lived. Possibly, SLSNe I exhibit a range of explosion timescales and therefore initial masses. More examples of extreme-starburst host-galaxy systems, and a better measurement of their true frequency, will be needed to resolve this.

6.6. The Absolute Efficiency of SLSNe in the Most Metal-poor Galaxies

The *absolute* rate of SLSNe also provides a constraint on progenitor models (Chen et al. 2013). For example, exotic scenarios involving a series of low-probability events could be ruled out if they do not produce enough SLSNe in the universe to explain the numbers that we observe. Or, a simple model in which an initial mass above a certain value is the *only* criterion can be ruled out if that value implies the production of too *many* SLSNe compared to the observed rate. Such constraints can in principle be strengthened by factoring in host-galaxy preferences: since most SLSNe I originate from a small subset of the overall galaxy population, the fraction of stars exploding as SLSNe in this type of galaxy is significantly higher than the "cosmic average" would suggest.

The overall average cosmic rate is constrained only very approximately at present. Quimby et al. (2013) previously estimated the SLSN I rate density at $z \approx 0.15$ to be roughly within the range of 10^1–10^2 events Gpc^{-3} yr^{-1}, compared to an overall CCSN rate of $\sim 10^5$ at the same redshift (e.g., Strolger et al. 2015): i.e., SLSNe I represent 1 out of every 10^3 to 10^4 SNe at this epoch.

This figure averages together the rate from metal-poor dwarf galaxies (which produce almost all of the SLSNe I) with the massive, metal-rich hosts (which produce almost none of them). Given the "step"-like behavior of the SLSN I rate we infer (as a function of mass and probably of metallicity; Figure 7), it makes sense to calculate separately the fraction in low-mass versus high-mass galaxies. This can be determined simply by multiplying the "average" number above by the values plotted in the bottom panel of Figure 7. In galaxies with masses below $10^9 M_\odot$, the fraction is higher by a factor of 5: SLSNe I constitute 1 per 200–2000 SNe. In galaxies with masses above $10^{10} M_\odot$, the fraction is instead *lower* by a factor of 5 (or more if 10uhf is ignored): SLSNe I constitute 1 per (>) 5000–50,000 SNe.

Given the rarity of extremely massive stars, a relatively high SLSN rate becomes interesting for constraining high-mass progenitor models. For example, if the SLSN I rate is at the high end of the Quimby et al. (2013) estimate (10^2 Gpc^{-3} yr^{-1}), then at $Z < 0.5 Z_\odot$ SLSNe I constitute 0.5% of all core-collapse SNe, 5% of SNe from progenitors with $M_{init} > 50 M_\odot$, and $\sim 50\%$ of SNe from progenitors with $M_{init} > 200 M_\odot$. (We use a high-end IMF slope of $\alpha = 2.3$ and assume that all stars with $M_{init} > 8 M_\odot$ explode as SNe.) The similarity of the SLSN rate to the high-mass star SN rate is particularly intriguing. If the intrinsic SLSN rate is at the low end of the Quimby et al. estimate, all these rates would drop by a factor of 10 and additional factors beyond mass and metallicity would become necessary to explain the SLSN rate *even if* the progenitor is extremely massive.

7. CONCLUSIONS

The hosts of SLSNe I have highly divergent properties from the general star-forming galaxy distribution: lower masses and metallicities (in nearly all cases) and unusually high specific SFRs (in a notable minority of cases). These trends do not appear to be due to selection effects and suggest a progenitor whose production is intrinsically favored in some environments and suppressed in others. Most likely, the primary factor influencing this is a requirement of low (but not extreme) metallicity: below a galaxy-averaged oxygen abundance of 12 $\log_{10}[O/H] \lesssim 8.4$ (equivalent to $0.5 Z_\odot$) the SLSN I rate rises by approximately a factor of 20 higher compared to galaxies with metallicities higher than this value. The rates of SLSNe I in metal-poor galaxies at $z \sim 0.2$ are about a factor of 5 higher than what would be implied by their cosmic "average."

A metallicity limit alone appears to provide good consistency with all of the bulk properties of the SLSN I host population without a need to introduce other factors (such as a dependence on specific SFR), and the observed abundance of SLSNe I in starbursting galaxies may simply reflect the bursty star formation histories of metal-poor, low-mass ($\sim 10^8 M_\odot$) galaxies. This comparison is limited by our small sample size and by the lack of large volume-complete spectroscopic surveys of nearby dwarf galaxies, however. In any case, the majority of SLSNe I in our sample occupy host galaxies with SFRs typical of their stellar masses, indicating that the role of an sSFR-dependent IMF or dynamical interactions is at best secondary.

The functional dependence of SLSNe I on metallicity we prefer is qualitatively similar to what has been inferred by recent work on GRBs: a constant or slowly variable rate up to a threshold, above which it drops sharply. However, the threshold for SLSNe ($\sim 0.5 Z_\odot$) appears to be lower than for GRBs ($\sim 1 Z_\odot$), so this similarity does not necessarily argue for a common origin. In any case, no first-principles progenitor model that we are aware of predicts the type of metallicity dependence that we infer for either transient, and more theoretical work is necessary to explain why the rates of energetic transients at $0.4 Z_\odot$ (SLSNe and GRBs common), $0.7 Z_\odot$ (only GRBs common), and $1.5 Z_\odot$ (neither event common) appear to be so dramatically different despite differences of factors of only a few in metal abundances.

While this behavior is theoretically puzzling, observationally it may render the problem more tractable: the relatively high metallicity threshold we infer, as well as the relatively "ordinary" nature of most host galaxies, suggests that the SMC and quite possibly the LMC are quite viable SLSN (and GRB) hosts. While the possibility of an actual SLSN occurring

in one of these galaxies anytime in the near future is of course miniscule, they may contain stars that are SLSN progenitors. Even if not, resolved-population studies will allow direct investigation into the differences of massive stellar populations over the range of metallicities relevant to controlling SLSN I production. Interestingly, there are already some indications from resolved studies that the LMC can form stars at $>200\,M_\odot$ but the Milky Way cannot (Crowther et al. 2010, 2016). If the progenitor of SLSNe I is indeed a very massive ($M_{\rm init} > 200\,M_\odot$) star, this may indicate that the manner by which metallicity affects SLSN production has more to do with massive star *formation* rather than massive star *evolution*.

All of the trends we discuss above are weaker, or absent entirely, among SLSNe II. While we find a modest tendency for SLSNe II to favor lower-mass hosts compared to cosmic star formation generally, this effect is not strong and some of it may be attributable to selection effects. A larger Type II host sample will be needed to resolve this question unambiguously, but we suggest that most SLSNe II likely represent a rare but not particularly environmentally dependent extreme of the same physical process that generates "ordinary" SNe IIn. The circumnuclear SLSNe represented by SN 2006gy and PTF 10tpz seem to represent a different situation entirely: these objects likely belong to a distinct class of transient, exclusive to these environments.

Recently, the ASAS-SN team announced the discovery of what they refer to as the "brightest supernova ever" (Dong et al. 2016). This event is reported to be of Type I and is located at the centroid of an extremely massive and red galaxy with no star formation present. Given the host-galaxy properties of SLSNe I (and even SLSNe II) within our own sample, we are skeptical that this event represents a genuine SLSN and suggest that it is more likely a tidal disruption event due to a star falling into the central black hole (the black hole in this galaxy would have to be unusually small given the galaxy's mass for a TDE to be observable, but this could be the case because of a dual SMBH from a minor merger, for example). If it is a genuine SN, it would suggest that whatever peculiar factors govern star formation near the centers of massive galaxy nuclei can favor SLSNe I and SLSNe II.

REFERENCES

Alam, S., Albareti, F. D., Allende Prieto, C., et al. 2015, ApJS, 219, 12
Angus, C. R., Levan, A. J., Perley, D. A., et al. 2016, MNRAS, 458, 84
Arcavi, I., Gal-Yam, A., Kasliwal, M. M., et al. 2010, ApJ, 721, 777
Arcavi, I., Gal-Yam, A., Sullivan, M., et al. 2014, ApJ, 793, 38
Arcavi, I., Wolf, W., Howell, A., et al. 2016, ApJ, 819, 35
Baldwin, J. A., Phillips, M. M., & Terlevich, R. 1981, PASP, 93, 5
Bamford, S. P., Rojas, A. L., Nichol, R. C., et al. 2008, MNRAS, 391, 607
Barkat, Z., Rakavy, G., & Sack, N. 1967, PhRvL, 18, 379
Benetti, S., Nicholl, M., Cappellaro, E., et al. 2014, MNRAS, 441, 289
Bergvall, N., Marquart, T., Way, M. J., et al. 2016, A&A, 587, A72
Bianco, F. B., Modjaz, M., Oh, S. M., et al. 2016, A&C, 16, 54
Brinchmann, J., Charlot, S., White, S. D. M., et al. 2004, MNRAS, 351, 1151

Brink, H., Richards, J. W., Poznanski, D., et al. 2013, MNRAS, 435, 1047
Bruzual, G., & Charlot, S. 2003, MNRAS, 344, 1000
Calzetti, D., Armus, L., Bohlin, R. C., et al. 2000, ApJ, 533, 682
Cameron, E. 2011, PASA, 28, 128
Cenko, S. B., Fox, D. B., Moon, D.-S., et al. 2006, PASP, 118, 1396
Chabrier, G. 2003, PASP, 115, 763
Chatzopoulos, E., Wheeler, J. C., Vinko, J., Horvath, Z. L., & Nagy, A. 2013, ApJ, 773, 76
Chen, T.-W., Smartt, S. J., Bresolin, F., et al. 2013, ApJL, 763, L28
Chen, T.-W., Smartt, S. J., Jerkstrand, A., et al. 2015, MNRAS, 452, 1567
Chen, T.-. W., Smartt, S. J., Yates, R. M., et al. 2016, arXiv:1605.04925
Chevalier, R. A., & Irwin, C. M. 2011, ApJL, 729, L6
Chornock, R., Berger, E., Gezari, S., et al. 2014, ApJ, 780, 44
Cohen, M., Wheaton, W. A., & Megeath, S. T. 2003, AJ, 126, 1090
Cook, D. O., Dale, D. A., Johnson, B. D., et al. 2014a, MNRAS, 445, 881
Cook, D. O., Dale, D. A., Johnson, B. D., et al. 2014b, MNRAS, 445, 899
Crowther, P. A., Caballero-Nieves, S. M., Bostroem, K. A., et al. 2016, MNRAS, 458, 624
Crowther, P. A., Schnurr, O., Hirschi, R., et al. 2010, MNRAS, 408, 731
Cutri, R. M., Wright, E. L., Conrow, T., et al. 2013, yCat, 2328
Dale, D. A., Cohen, S. A., Johnson, L. C., et al. 2009, ApJ, 703, 517
Dark Energy Survey Collaboration 2016, MNRAS, 460, 1270
Denicoló, G., Terlevich, R., & Terlevich, E. 2002, MNRAS, 330, 69
Dessart, L., Hillier, D. J., Waldman, R., Livne, E., & Blondin, S. 2012, MNRAS, 426, L76
Dong, S., Shappee, B. J., Prieto, J. L., et al. 2016, Sci, 351, 257
Drake, A. J., Djorgovski, S. G., Mahabal, A., et al. 2009, ApJ, 696, 870
Drake, A. J., Djorgovski, S. G., Mahabal, A., et al. 2011, ApJ, 735, 106
Drout, M. R., Chornock, R., Soderberg, A. M., et al. 2014, ApJ, 794, 23
Faber, S. M., Phillips, A. C., Kibrick, R. I., et al. 2003, Proc. SPIE, 4841, 1657
Filippenko, A. V. 1982, PASP, 94, 715
Filippenko, A. V. 1989, AJ, 97, 726
Filippenko, A. V. 1997, ARA&A, 35, 309
Filippenko, A. V., Li, W. D., Treffers, R. R., & Modjaz, M. 2001, in ASP Conf. Ser. 246, IAU Coll. 183: Small Telescope Astronomy on Global Scales, ed. B. Paczynski, W.-P. Chen, & C. Lemme (San Francisco, CA: ASP), 121
Fukugita, M., Shimasaku, K., & Ichikawa, T. 1995, PASP, 107, 945
Gal-Yam, A. 2012, Sci, 337, 927
Gal-Yam, A., Mazzali, P., Ofek, E. O., et al. 2009, Natur, 462, 624
Gezari, S., Halpern, J. P., Grupe, D., et al. 2009, ApJ, 690, 1313
Gilkis, A., Soker, N., & Papish, O. 2015, arXiv:1511.01471
Ginzburg, S., & Balberg, S. 2012, ApJ, 757, 178
Graham, J. F., & Fruchter, A. S. 2013, ApJ, 774, 119
Hadjiyska, E., Rabinowitz, D., Baltay, C., et al. 2012, in IAU Symp. 285, ed. E. Griffin, R. Hanisch, & R. Seaman, 324
Heger, A., Fryer, C. L., Woosley, S. E., Langer, N., & Hartmann, D. H. 2003, ApJ, 591, 288
Inserra, C., Smartt, S. J., Gall, E. E. E., et al. 2016, arXiv:1604.01226
Inserra, C., Smartt, S. J., Jerkstrand, A., et al. 2013, ApJ, 770, 128
Izotov, Y. I., Stasińska, G., Meynet, G., Guseva, N. G., & Thuan, T. X. 2006, A&A, 448, 955
Japelj, J., Vergani, S. D., Salvaterra, R., et al. 2016, A&A, 590, A129
Jerkstrand, A., Smartt, S. J., & Heger, A. 2016, MNRAS, 455, 3207
Kaiser, N., Aussel, H., Burke, B. E., et al. 2002, Proc. SPIE, 4836, 154
Kasen, D., & Bildsten, L. 2010, ApJ, 717, 245
Keller, S. C., Schmidt, B. P., Bessell, M. S., et al. 2007, PASA, 24, 1
Kennicutt, R. C., Jr., Lee, J. C., Funes, J. G., et al. 2008, ApJS, 178, 247
Kennicutt, R. C., Jr., Roettiger, K. A., Keel, W. C., van der Hulst, J. M., & Hummel, E. 1987, AJ, 93, 1011
Kewley, L. J., & Dopita, M. A. 2002, ApJS, 142, 35
Kiewe, M., Gal-Yam, A., Arcavi, I., et al. 2012, ApJ, 744, 10
Kobulnicky, H. A., & Kewley, L. J. 2004, ApJ, 617, 240
Kobulnicky, H. A., & Skillman, E. D. 1997, ApJ, 489, 636
Kodros, J., Cenko, S. B., Li, W., et al. 2010, CBET, 2461, 1
Krühler, T., Malesani, D., Fynbo, J. P. U., et al. 2015, A&A, 581, A125
Langer, N., Norman, C. A., de Koter, A., et al. 2007, A&A, 475, L19
Law, N. M., Kulkarni, S. R., Dekany, R. G., et al. 2009, PASP, 121, 1395
Lee, J. C., Gil de Paz, A., Kennicutt, R. C., Jr., et al. 2011, ApJS, 192, 6
Lee, J. C., Kennicutt, R. C., Jr., Funes, S. J. J. G., Sakai, S., & Akiyama, S. 2009, ApJ, 692, 1305
Leloudas, G., Chatzopoulos, E., Dilday, B., et al. 2012, A&A, 541, A129
Leloudas, G., Fraser, M., Stone, N. C., et al. 2017, arXiv:1609.02927
Leloudas, G., Gallazzi, A., Sollerman, J., et al. 2011, A&A, 530, A95
Leloudas, G., Schulze, S., Krühler, T., et al. 2015, MNRAS, 449, 917
Li, W., Leaman, J., Chornock, R., et al. 2011, MNRAS, 412, 1441

Lunnan, R., Chornock, R., Berger, E., et al. 2013, ApJ, 771, 97
Lunnan, R., Chornock, R., Berger, E., et al. 2014, ApJ, 787, 138
Lunnan, R., Chornock, R., Berger, E., et al. 2015, ApJ, 804, 90
Maiolino, R., Nagao, T., Grazian, A., et al. 2008, A&A, 488, 463
Mannucci, F., Cresci, G., Maiolino, R., Marconi, A., & Gnerucci, A. 2010, MNRAS, 408, 2115
Marble, A. R., Engelbracht, C. W., van Zee, L., et al. 2010, ApJ, 715, 506
Marchant, P., Langer, N., Podsiadlowski, P., Tauris, T. M., & Moriya, T. J. 2016, A&A, 588, A50
Marino, R. A., Rosales-Ortega, F. F., Sánchez, S. F., et al. 2013, A&A, 559, A114
Mazzali, P. A., Deng, J., Nomoto, K., et al. 2006, Natur, 442, 1018
McCrum, M., Smartt, S. J., Rest, A., et al. 2015, MNRAS, 448, 1206
McLean, I. S., Steidel, C. C., Epps, H. W., et al. 2012, Proc. SPIE, 8446, 0
McQuinn, K. B. W., Skillman, E. D., Cannon, J. M., et al. 2010, ApJ, 724, 49
Metzger, B. D., Margalit, B., Kasen, D., & Quataert, E. 2015, MNRAS, 454, 3311
Miller, A. A., Chornock, R., Perley, D. A., et al. 2009, ApJ, 690, 1303
Modjaz, M., Kewley, L., Kirshner, R. P., et al. 2008, AJ, 135, 1136
Moriya, T. J., Blinnikov, S. I., Tominaga, N., et al. 2013, MNRAS, 428, 1020
Muzzin, A., Marchesini, D., Stefanon, M., et al. 2013, ApJS, 206, 8
Nagao, T., Maiolino, R., & Marconi, A. 2006, A&A, 459, 85
Neill, J. D., Sullivan, M., Gal-Yam, A., et al. 2011, ApJ, 727, 15
Nicholl, M., Smartt, S. J., Jerkstrand, A., et al. 2013, Natur, 502, 346
Nicholl, M., Smartt, S. J., Jerkstrand, A., et al. 2015, MNRAS, 452, 3869
Niino, Y. 2011, MNRAS, 417, 567
Ofek, E. O., Arcavi, I., Tal, D., et al. 2014, ApJ, 788, 154
Ofek, E. O., Cameron, P. B., Kasliwal, M. M., et al. 2007, ApJL, 659, L13
Oke, J. B., Cohen, J. G., Carr, M., et al. 1995, PASP, 107, 375
Oke, J. B., & Gunn, J. E. 1983, ApJ, 266, 713
Pagel, B. E. J., Edmunds, M. G., Blackwell, D. E., Chun, M. S., & Smith, G. 1979, MNRAS, 189, 95
Pan, T., Loeb, A., & Kasen, D. 2012, MNRAS, 423, 2203
Peng, C. Y., Ho, L. C., Impey, C. D., & Rix, H.-W. 2002, AJ, 124, 266
Perley, D. A., Levan, A. J., Tanvir, N. R., et al. 2013, ApJ, 778, 128
Perley, D. A., Tanvir, N. R., Hjorth, J., et al. 2016, ApJ, 817, 8
Pettini, M., & Pagel, B. E. J. 2004, MNRAS, 348, L59
Phillips, A. C., Miller, J., Cowley, D., & Wallace, V. 2006, Proc. SPIE, 6269, 1
Quimby, R. M., Kulkarni, S. R., Kasliwal, M. M., et al. 2011, Natur, 474, 487
Quimby, R. M., Yuan, F., Akerlof, C., & Wheeler, J. C. 2013, MNRAS, 431, 912
Rahmer, G., Smith, R., Velur, V., et al. 2008, Proc. SPIE, 7014, 4
Rakavy, G., & Shaviv, G. 1967, ApJ, 148, 803
Richardson, D., Branch, D., Casebeer, D., et al. 2002, AJ, 123, 745
Sanders, N. E., Soderberg, A. M., Levesque, E. M., et al. 2012, ApJ, 758, 132
Sanders, R. L., Shapley, A. E., Kriek, M., et al. 2015, ApJ, 799, 138
Schlafly, E. F., & Finkbeiner, D. P. 2011, ApJ, 737, 103
Schlegel, E. M. 1990, MNRAS, 244, 269
Shappee, B. J., Prieto, J. L., Grupe, D., et al. 2014, ApJ, 788, 48
Silverman, J. M., Nugent, P. E., Gal-Yam, A., et al. 2013, ApJS, 207, 3
Smith, N., Chornock, R., Silverman, J. M., Filippenko, A. V., & Foley, R. J. 2010, ApJ, 709, 856
Smith, N., Li, W., Foley, R. J., et al. 2007, ApJ, 666, 1116
Soker, N. 2016, NewA, 47, 88
Stanek, K. Z., Gnedin, O. Y., Beacom, J. F., et al. 2006, AcA, 56, 333
Strauss, M. A., Weinberg, D. H., Lupton, R. H., et al. 2002, AJ, 124, 1810
Strolger, L.-G., Dahlen, T., Rodney, S. A., et al. 2015, ApJ, 813, 93
Thöne, C. C., de Ugarte Postigo, A., García-Benito, R., et al. 2015, MNRAS, 451, L65
Usov, V. V. 1992, Natur, 357, 472
van den Heuvel, E. P. J., & Portegies Zwart, S. F. 2013, ApJ, 779, 114
van Dokkum, P. G. 2001, PASP, 113, 1420
Vergani, S. D., Salvaterra, R., Japelj, J., et al. 2015, A&A, 581, A102
Vreeswijk, P. M., Savaglio, S., Gal-Yam, A., et al. 2014, ApJ, 797, 24
Waldman, R. 2008, ApJ, 685, 1103
Walsh, J. R., & Roy, J.-R. 1993, MNRAS, 262, 27
Woosley, S. E. 2010, ApJL, 719, L204
Woosley, S. E., Blinnikov, S., & Heger, A. 2007, Natur, 450, 390
Wright, E. L., Eisenhardt, P. R. M., Mainzer, A. K., et al. 2010, AJ, 140, 1868
Yan, L., Quimby, R., Ofek, E., et al. 2015, ApJ, 814, 108
Yaron, O., & Gal-Yam, A. 2012, PASP, 124, 668
Yoshida, T., Okita, S., & Umeda, H. 2014, MNRAS, 438, 3119
Yoshida, T., & Umeda, H. 2011, MNRAS, 412, L78
Yusof, N., Hirschi, R., Meynet, G., et al. 2013, MNRAS, 433, 1114
Zahid, H. J., Dima, G. I., Kudritzki, R.-P., et al. 2014, ApJ, 791, 130